Advances in three-dimensional graphene-based materials: configurations, preparations and applications in secondary metal (Li, Na, K, Mg, Al)-ion batteries

Guangzhe Li[†,1], Bin Huang[†,1], Zhefei Pan[1], Xiangyu Su[1], Zongping Shao*[,2,3], Liang An*[,1]

[1] Department of Mechanical Engineering, The Hong Kong Polytechnic University, Hung Hom, Kowloon, Hong Kong SAR, China

[2] Jiangsu National Synergetic Innovation Center for Advanced Material College of Energy & State Key Laboratory of Materials-Oriented Chemical Engineering, Nanjing Tech University, Nanjing 210009, China

[3] Department of Chemical Engineering, Curtin University, Perth, WA 6845, Australia

[†] Equal contribution.

[*] Corresponding authors.

Email: zongping.shao@curtin.edu.au (Z.P. Shao)

Email: liang.an@polyu.edu.hk (L. An)

Abstract

Three-dimensional (3D) graphene materials, consisting of unstacked two-dimensional (2D) graphene sheets serving as building blocks, have been widely reported in recent years. Various synthetic methods have been employed to prepare graphene materials with diverse 3D architectures, which show potential in wide applications such as energy and environmental technologies. In particular, the applications of 3D graphene-based materials in metal (Li, Na, K, Mg, Al)-ion battery (MIB) system have been numerously reported in recent years. However, the critical roles of 3D graphene materials in MIB systems have not been comprehensively discussed. Herein, we first summarize the configurations and preparations of 3D graphene materials. Second, we illustrate the metal-ion storage mechanisms in graphene layers, i.e. intercalation and adsorption. Third, we emphasize superior functionalities of 3D graphene architectures as supporting and encapsulating materials in MIB applications. Last, we discuss merits and drawbacks of various 3D graphene architectures in MIB systems. We aim to present a comprehensive understanding of 3D graphene materials and guide directions for future MIB designs.

Keywords: Three-dimensional graphene; Metal-ion batteries; Intercalated sites; Adsorption surface; Supporting materials; Encapsulating materials

1. Introduction

Graphene, with intrinsic two-dimensional (2D) structure containing honeycomb-like carbon atoms, possesses extraordinary physicochemical properties, such as high thermal conductivity, high carrier mobility and good optical transparency.[1] In order to achieve its practical use, the assembly of graphene layers into a macroscopic level is required. Here, 3D graphene materials, by our definition, are built from unstacked 2D graphene sheets serving as building blocks.[2] They have received tremendous attentions during the past years, since they not only inherit the outstanding properties of 2D graphene sheets, but also provide novel functions for energy storage and environmental applications.[3–5] Up to now, 3D graphene materials with diverse architectures have been synthesized, including graphene balls,[6] graphene fibers,[7] graphene tubes,[8] graphene scrolls,[9] graphene networks,[10] graphene vertical sheets,[11] graphene cages,[12] and graphene with other 3D architectures.[13] To obtain all these architectures, various synthetic methods have been employed, which can be generally classified as chemical vapor deposition (CVD) method,[8,10,14] self-assembly method,[15–18] and other methods.[19,20] In order to tune the structures and properties of 3D graphene materials in synthetic procedure, templates are often used such as nickel foam and silica particles.[21] The obtained 3D graphene materials with targeted designs show promises in various applications for energy storage, such as supercapacitors,[22] lithium-ion batteries (LIBs),[23] sodium-ion batteries (SIBs).[24]

Lithium-ion battery is one of the most popular electrochemical energy storage devices and its industry grew rapidly in the last thirty years. However, due to the limited lithium resources in earth crust, LIBs may not meet the demands of sustainable developments. In this regard, other metal (Na, K, Mg and Al)-ion batteries (MIBs) have been developed, which show great promises due to the large resource reserve of metals

and compelling energy density as compared to LIBs. In recent years, there are increasing studies on the applications of 3D graphene materials in MIBs.[25,26] In their studies, basically, there are two functions of 3D graphene materials: one is working as metal-host materials to store metal ions effectively in graphene layers; the other is working as matrix to form 3D composite architectures.

3D graphene materials are promising metal-host materials for MIB applications. Metal ions, including Li^+, Na^+, K^+, Al^{3+}, can intercalate into graphene layers or/and adsorb on the surface.[27] In addition, the graphene sheets with defective structures or heteroatoms dopants offer enhanced ion adsorption effect, since metal ions can bind with defect sites such as edges[28] and surface heteroatoms such as boron[29] by Faradic reactions. Compared to conventional metal-ion storage via intercalation, such Faradic reactions offer a capacitive behavior, showing much faster ion diffusion kinetics and thus improving rate capabilities of electrode materials.[30]

3D graphene architectures offer structural superiorities in fabricating 3D composite electrodes.[31] The diversities, tunabilities and functionalities of 3D graphene architectures enable rational designs of composite electrodes for MIB applications. For example, 3D graphene network contains interconnected graphene sheets and offers highly porous structure. Its conductive network can serve as highways for electrons transmission, and its porous structure enables electrolyte filtration, which accelerates ions transport by reducing ion diffusion distance.[32] In the meantime, intrinsic physical properties of graphene sheets like high specific surface area, robustness and flexibility are suitable for supporting other metal-host materials to fabricate advanced composite electrodes. Therefore, metal-host material@3D graphene network electrodes can present enhanced electron and ion transport, resulting in improved metal-ion storage properties. In addition, some 3D graphene architectures like graphene spheres and

graphene cages possess configuration advantages, which can not only enhance electrons and ions transport but also construct an enclosure structure to buffer or accommodate the volume expansion of metal-host materials during cycling.[12] As a result, the improved cyclic stability can be achieved owing to less structural degradation of metal-host materials. Other 3D graphene architectures like graphene vertical sheets, with a large amount of exposed edges, can also improve the power densities of LIBs by accelerating local ion diffusion at edge sites.

Up to now, there are a few review articles related to 3D graphene materials available in the open literature.[33,34,43–46,35–42] Particularly, the progress has been scattered in several reviews with a focus on preparation methods such as self-assembly,[33–35] CVD methods,[36] or with emphasis on structures such as graphene sponge,[3] graphene network,[37] graphene spheres,[38] or focusing on specific applications such as supercapacitors,[33,39,40] catalysis,[41,42] LIBs.[43–46] In addition to LIBs, the progress of other MIBs (Na, K, Mg, Al) is also remarkable.[23,47,56–58,48–55] A timely and comprehensive review focusing on MIB applications is thus deemed necessary.

In this review, we summarize the preparations and configurations of 3D graphene-based materials and specify their applications in various MIBs. We emphasize significant roles of graphene layers, serving as intercalation sites and adsorption surface. We further discuss superior functionalities of 3D graphene architectures as supporting materials and encapsulating materials in MIB applications. In addition, we also discuss the merits and drawbacks of applying different 3D graphene architectures as metal-host materials and matrix in MIB systems. At the end, we summarize the challenging issues that still remain and give future research directions.

2. 3D graphene architectures

2.1 Graphene spheres

Graphene spheres (graphene balls) refer to a type of 3D graphene materials with hollow and spherical secondary structure. There are mainly two types of graphene spheres divided by their surface morphologies. One is called crumpled graphene balls (CGBs), with many ridges and vertices on their surface. CGBs were first successfully prepared via evaporating aerosol droplets method.[6] Specifically, as shown in Fig. 1a, graphene oxide (GO) suspension was nebulized to form aerosol droplets, followed by rapid evaporation. CGBs were thus formed due to the shrinkage of the droplets under hydrostatic pressure. The size of CGBs was in the sub-micrometer range (Fig. 1b-g), which could be tuned by adjusting the concentration of GO suspension. The other type of graphene balls (GBs) with relatively smooth surface morphologies can be prepared via template-assisted method. For example, graphene balls were successfully grown on nickel nanoparticles (NPs) via carburization and segregation.[59] The hollow graphene balls inherited the spherical structure of NPs, which served as the sacrificing template. Apart from NPs, other hard templates were also used to prepare GBs, such as silica spheres,[60,61] polymethylmethacrylate (PMMA) spheres,[62] polystyrene spheres[63] and MgAl layered double oxide spheres.[64] The diameter of GBs was in a wide range from nanometers to micrometers, depending on the template structures. In addition, soft templates such as water droplets could also assist the construction of GBs.[65,66] A water-in-oil (W/O) emulsion technique was reported to prepare hollow graphene oxide spheres (HGOS).[65] In the preparation, the GO nanosheets would first restack around the water droplets due to their hydrophilic properties; Then, by removal of water and oil, HGOS with a diameter in the range of 2-10 micrometers were obtained. By tailoring synthetic conditions, the surface of HGOS could be either irregular and rough, or

uniform and smooth. Graphene spheres with aggregation-resistant property find potential applications in energy storage and conversion such as fuel cells[67] and supercapacitors.[68] In addition, their highly reactive edges also offer novel functions such as adsorptions[69] and friction reductions.[70]

2.2 Graphene fibers, tubes and scrolls

Graphene fibers can be prepared by assembling GO sheets into fiber-type structures. Recently, light, flexible and multifunctional graphene fibers were successfully prepared by dimensionally confined hydrothermal method.[7] GO suspension was first injected into glass pipeline, followed by hydrothermal reaction at 230 ºC. The obtained graphene fiber had a linear structure with a diameter of 33 micrometers. Owing to the densely stacked graphene sheets along the fiber axis, the textile strength of graphene fiber could reach up to 420 MPa, showing excellent mechanical properties. Cao et al. reported the preparation of ultra-strong graphene fibers with superior tensile strength (0.5 GPa).[71] They were prepared by self-assembly method, by using giant GO sheets with high aspects ratios as building blocks. The diameter of the obtained fibers was as thin as 6 micrometers and the section morphology showed a origami-flower-like microstructure, in which graphene sheets were partially aligned and densely stacked with each other. In addition, the obtained graphene fibers also possessed excellent electronic conductivity ($3.8\text{-}4.1\times10^4$ S m^{-1}). Graphene fibers showed potentials in multiple devices, including flexible fiber-type actuators, motors, photovoltaic cells, as well as supercapacitors.[72,73]

Graphene tubes, with a typical tubular structure and a larger diameter compared to single-wall carbon nanotubes (2-5 nm), were successfully prepared via template-assisted CVD method.[8,74] Nickel nanowires were reported as both the sacrificing template and the catalyst to prepare graphene nanotubes.[8] The wall of graphene tubes contains several graphene layers, and the number of graphene layers can be tailored by

adjusting the growth time. Graphene tubes were grown on the porous anodic aluminum oxide (AAO) template by carbothermic reduction reaction.[74] They had one-dimensional tubular structure and the diameter of a single tube was about 110 nm. The obtained graphene tubes could act as a medium for directional heat transport. In another work, graphene/graphene tubes composite was prepared by carbonizing dicyandiamide (DCDA) in the presence of iron species.[75] The graphene nanotubes had no distinct orientations and the diameter of nanotubes shows a wide range, from tens of nanometers to sub-micrometer. Similarly, bamboo-like nitrogen doped graphene tubes were also prepared by high graphitization process of DCDA.[76] The length of tubes was up to tens of micrometers, and the diameter of the tubes was sub-micrometer. Large size of graphene tubes could facilitate the anchoring of Pt nanoparticles and Pt nanoparticles anchoring on graphene tubes showed excellent oxygen reduction reaction (ORR) activity.

Graphene scrolls (carbon nanoscrolls), with a linear and tubular structure similar to multi-wall carbon nanotubes (MWCNTs), were also prepared.[77,78] MWCNTs possess a coaxial tube structure, containing several to dozens of intact carbon atom layers with hexagonal arrangement, with no exposed edges along the axial direction. Differently, graphene scrolls contain scrolled graphene layers with both open ends and edges along the axial direction. They were first prepared by a chemical route.[9] The potassium-ion compound was first intercalated into graphite under helium atmosphere to assist the exfoliation of graphite into separated graphene sheets. The following sonication treatment could induce scrolling of graphene sheets. The average diameter and length of graphene scrolls were about 40 nm and 1.3 μm, respectively. They also had relatively large surface area contributed by their open ends, compared to the sealed carbon nanotubes. This unique structure shows promises for multiple applications such as

adsorption, hydrogen storage and energy storage. Graphene scrolls were also prepared by microexplosion method.[77] Typically, Mn^{2+} was first infiltrated into the interlayer of GO sheets, followed by reacting with $KMnO_4$ to obtain MnO_2/GO composites. After adding H_2O_2, a large amount of oxygen was generated by H_2O_2 decomposition. The quick release of gas induced the exfoliation and scrolling of GO sheets. Finally, graphene scrolls were obtained after the chemical reduction and removal of solvent. The preparation enables the formation of different structures including one-side nanoscrolls, diagonal nanoscrolls and two-sided nanoscrolls, as shown in Fig. 2a.[78] The diameter of the obtained graphene scrolls was in the range of 20 to 100 nm (Fig. 2b-e). Graphene scrolls with excellent electrochemical properties show great promise for applications such as supercapacitors[78] and hydrogen evolution.[79]

2.3 Vertical graphene sheets

Vertical graphene sheets (VGS), also called carbon nanowalls (CNWs), have a unique structure with interconnected 3D network, open channels as well as thin and exposed edges.[11,80–82] VGS grown on the substrate are tightly fixed and show a highly directional orientation vertical to the substrate. Plasma enhanced chemical vapor method (PECVD) was mostly reported to prepare VGS.[83–87] Wu et al.[11] first reported the preparation of carbon nanowalls via PECVD method. By introducing mixture gases of methane and hydrogen into PECVD system, carbon nanowalls were grown on different substrates such as silicon, stainless steel and copper. Plasma could assist the vertical growth of nanocarbon layers with sharp edges, containing single graphene layer or folded double graphene layers. Hiramatsu et al.[80] also prepared carbon nanowalls via PECVD method but using different feedstocks including CF_4 and C_2F_6.

Although PECVD method was reported numerously, harsh conditions such as plasma sources were required to obtain high quality VGS.[88,89] In order to simplify the

preparation process, Zhao et al.[90] directly carbonized carbon nanofibers (CNFs) in ammonia to obtain VGS on their surface. The radially oriented VGS were formed due to preferential etching of ammonia on the circumferentially oriented graphite layer (Fig. 3a-d). The height of VGS protruding outward from CNFs was several nanometers. Based on this work, Zeng et al. reported that further growth of VGS could be realized via thermal CVD method.[91] The performed VGS on CNFs could act as nucleation sites or crystal seeds to facilitate the growth of VGS (Fig. 3f). By introducing methane and hydrogen gas in thermal CVD, further growth of VGS could be achieved, and the height of VGS was extended to 195 nm after four hours' growth (Fig. 3g-h). By prolonging the growth time, VGS could merge with each other, forming porous graphene (Fig. 3 i-j). The pore size was in the range from 20 to 100 nm, much smaller than the pore size of other porous graphene.[92,93] The obtained VGS showed high electrical conductivity (1.2×10^5 S m^{-1}), superhydrophobicity and high electromagnetic (EMI) shielding performance (60932 dB cm^2g^{-1}). The VGS could also be prepared by direct electrochemical anodization of graphite.[94] The dense array of VGS showed excellent areal capacitance (1.3 F cm^{-2}) as well as volumetric capacitance (3.9 F cm^{-3}) in supercapacitors.

2.4 Graphene networks

3D graphene networks are the most frequently reported 3D graphene architectures, and their mass production can be achieved via self-assembly method.[95–98] For example, graphene hydrogel was successfully prepared via one-step hydrothermal method.[95] It had an interconnected porous network with randomly aligned sheets and the pore size was in the range of submicrometers to several micrometers. Qiu et al.[96] also reported the synthesis of highly compressible and ultralight graphene aerogel by chemical reduction of GO sheets. The obtained material had a foam-like structure with the pore

size ranging from tens to hundreds of micrometers.

Graphene networks prepared by self-assembly method often suffer from poor quality with abundant defects and intersheet junctions. CVD method is an effective approach to prepare 3D graphene network with high quality. Chen et al.[10] first reported the growth of graphene foam (GF) on the nickel foam. The obtained GF inherited the structure of the nickel foam and the graphene sheets were seamlessly interconnected. It also offered high conductivity (exceeding 10 S cm^{-1}), good mechanical properties and high specific surface area (850 m^2 g^{-1}).

3D graphene network shows potential for many applications such as LIBs[99] and sensors.[100] In addition, 3D graphene network can serve as a scaffold to prepare 3D graphene-based composites. Up to now, 3D graphene/metal oxides, 3D graphene/metal nanoparticles, 3D graphene/sulfide composites and 3D graphene/polymer composites have been prepared successfully,[101] enabling multiple applications such as electrocatalyst[102,103] and supercapacitor.[104]

2.5 Graphene cages

The construction of graphene cages with well-designed structures have been reported in recent years.[12,105,106] Owing to the robustness, flexibility and high conductivity of graphene nanosheets, they offer superior properties in energy storage. Recently, conformal graphene cages were grown on silicon particles as stable anodes for LIBs.[12] Nickel was coated on silicon particles for graphene growth and also as sacrificing template to create void space between silicon particles and graphene cages (Fig. 4a). The as-prepared graphene cages possessed a wavy structure along the nickel grains, as shown in Fig. 4b-d. This unique structure could buffer the volume change of silicon particles during lithiation. Graphene cages were also prepared by carbon segregation from nickel nanoparticles.[105] The pore size of graphene cages was in the

range of 1 - 3 μm and the wall thickness was in the range of 20-30 nm. The graphene cages owned multiple functions in constructing electrodes for lithium-sulfur batteries, including enhancing the electron transfer and providing a physical barrier to confine polysulfides. Very recently, 3D graphene cages encapsulating tin oxide nanoparticles were also prepared.[106] Sulfur served as the sacrificing template to create the void space between tin oxide and graphene cages. After the growth of graphene cage and template removal, the outer contour of graphene cage was identical to that of the inner tin oxide particles. By simply adjusting sulfur concentration, the volume of the void space could be tuned, as shown in Fig. 4e-f. As a result, graphene cages encapsulating tin oxides, as anodes in LIBs, exhibited an ultrahigh volumetric energy density (2123 mA h cm^{-3}) and also good cyclic performance.

2.6 Other types of 3D graphene

3D graphene with flower-like structure, honeycomb-like structure and hollow-cube structure were also reported.[13,107,108] For example, 3D graphene with honeycomb-like architecture was synthesized via a simple reaction between Li_2O and CO, as shown in Equation 1.[13]

$$Li_2O\ (s) + 2CO\ (g) \rightarrow C\ (graphene)\ (s) + Li_2CO_3\ (s) \quad (1)$$

The simultaneously formed Li_2CO_3 can prevent the combination of graphene nanosheets into graphite. The obtained 3D graphene had a honeycomb-like structure and the cell size lied in the range of 50-500 nm. It showed high efficiency as catalyst for dye sensitized solar cells comparable to Pt electrode. 3D graphene with flower-like structure was also fabricated via a simple reaction between Li (liquid) and CO_2, as shown in Equation 2.[107] Li liquid was reacted with CO_2 at 550 °C, followed by removal of Li_2CO_3.

$$4Li\ (l) + 3CO_2\ (g) \rightarrow C\ (graphene)\ (s) + 2Li_2CO_3\ (s) \quad (2)$$

The obtained 3D graphene materials had a cauliflower-fungus-shape structure with high porosity and exposed edges. They exhibited ultrahigh areal capacitance (up to 1.16 F cm^{-2}) as well as efficient mass loading (11.16 mg cm^{-2}) as electrode in supercapacitor.

The synthesis of graphene cubes with hollow structures was also reported recently.[108] Plasma-etched NaCl with regularly arranged cube-like microstructures was used as the sacrificing template. After CVD growth and template removal, graphene hollow cubes were obtained. The average length of single graphene cube unit was about 10 μm. The upper surface of cube units presented interconnected graphene network and the side surface of cube presented uneven stair-stepping graphene network. All the cube units were well connected with each other, offering good electrical conductivity. In addition, they also possessed high mechanical strength and large surface area. With these advantages, they exhibited high volumetric energy (657.2 mW h cm^{-3}) and power densities (954.3 mW cm^{-3}) as electrode in supercapacitor.

3. Preparation methods

3D graphene with different structures can be prepared by CVD method,[8,10] self-assembly method,[15–17,95,96] electrochemical exfoliation method,[94] blowing synthesis method,[109] etc. Among them, CVD and self-assembly are the two most frequently reported methods. Templates are also used in these methods to tune the pore structures of 3D graphene materials for various applications.[110,111,120–124,112–119] The preparation methods with and without the assistance of templates are reviewed as follows.

3.1 CVD method

CVD is an effective method to prepare graphene materials with good crystallization and few defects. Planar few-layered graphene was first prepared by thermal CVD in 2006.[125] Since then, the preparation of 3D graphene materials via CVD method has been widely reported.

3.1.1 Template-assisted CVD

In CVD process, templates were used to tune the structures and properties of 3D graphene materials. Nickel foam is suitable for constructing graphene networks due to its high porosity, interconnected framework and catalytic effect.[10] Self-standing graphene networks could be obtained after the removal of template. In addition, due to the excellent conductivity of nickel foam (350 S cm^{-1}), graphene network preserving the template can serve as free-standing electrode for energy storage applications.

Another commonly used template is silica spheres.[54,126] 3D graphene can inherit the structure of silica template and the removal of silica is required for constructing electrodes due to its insulation nature. Other templates including MOFs,[75] surface modified polystyrene balls,[127] porous copper,[128] MgO,[129] micro-structured NaCl[108] were also exploited to fabricate 3D graphene with diverse architectures. Their properties and applications are summarized in Table 1.

3.1.2 Non-template CVD

Non-template CVD with the assistance of plasma is able to prepare graphene vertical sheets, in which plasma contributes to the vertical growth of graphene sheets, forming 3D architectures.[84,87] The preparation of graphene fibers via non-template CVD method was also reported recently.[91] The graphene crystal seeds prepared beforehand and etching effect of introduced hydrogen account for the vertical growth of graphene sheets. Graphene sheets would merge with each other after long-time growth, forming 3D porous structure. This novel approach shows promise for the large-scale production of 3D graphene materials.

3.2 Self-assembly method

Self-assembly method is commonly used in GO suspension system to prepare 3D graphene materials. By breaking the equilibrium state of GO sheets in suspension under

certain conditions, GO sheets can link with each other spontaneously. After the reduction of GO, 3D graphene materials can be obtained.

3.2.1 Template-assisted self-assembly

Templates are often used to adjust the pore structures of 3D graphene materials during self-assembly process. For example, nickel foam is used to prepare 3D graphene materials with macroporous networks. Wang et al.[16] reported the successful preparation of reduced graphene oxide (rGO) network with sufficient mechanical strength, excellent conductivity and low density. Nickel foam was coated with GO via dip-coating, followed by electrochemical reduction and template removal. Melamine sponge[130] and polyurethane sponge[17] are also used as templates for the assembly of GO since they offer highly porous structure and are ease of removal. In addition, they can serve as supports to prevent the agglomeration of graphene sheets. For example, Yang et al.[17] prepared the graphene network with high specific area using polyurethane (PU) sponge as the template. The PU sponge was immersed into GO suspension, followed by thermal annealing to removal the template. The obtained graphene network exhibited ultrahigh capacitive deionization performance with excellent electrosorptive capacity of 4.95 mg g^{-1} and a fast desorption rate of 25 min.

Sulfur, with flowable, deformable and removable characteristics, could also serve as the template for the preparation of graphene cages. For example, tin oxide encapsulated by graphene cages was recently reported.[106] In this work, sulfur was employed as the sacrificing template to create void space between tin oxide and graphene cages.[106] Owing to the flowable property of sulfur, an intimate interfacial contact between tin oxide and sulfur was observed (Fig. 4f). By adjusting the original sulfur content to 21 %, optimal void space between tin oxide and graphene cages was preserved, resulting in a high volumetric energy density for lithium storage (Fig. 4e-g).

Other templates such as silica,[131] soap bubbles[92] and water droplets[65] were also used to prepare 3D graphene materials.

3.2.2 Non-template self-assembly method

3D graphene materials with random sheet-like structure can be prepared by non-template self-assembly method. Different techniques have been used to induce the self-assembly of GO sheets. Vacuum centrifugal technique is able to prepare graphene sponge.[132,133] Liu et al.[132] first reported the successful synthesis of graphene sponge in a large scale by evaporating colloidal GO suspensions. GO sheets were self-assembled in a layer-by-layer manner and their thickness can also be tuned by adjusting the concentration of GO suspension. After thermally annealing in Ar/H_2 mixture, the graphene sponge with 3D interconnected network was obtained. Similarly, by rapid evaporation of water droplets, CGBs could also be prepared.[38,134] In addition, electrochemical reduction[18] and chemical reduction by using agents such as ethylenediamine (EDA),[135,136] vitamin C[137–139] and hydrazine[140] are also effective in inducing self-assembly of GO sheets.

3.3 Other methods

3.3.1 Electrochemical exfoliation

Electrochemical exfoliation is a efficient and environmental friendly approach to prepare 3D graphene materials.[94,141,142] Zhang et al.[94] reported the exfoliation of graphite into GO in a two-electrode system. Natural graphite adhered on the copper wire was used as the anode and Pt foil was used as the cathode.[94] By applying a positive DC voltage, the graphite was partially oxidized into GO. After chemical reduction, rGO sheets anchored on graphite was obtained.

3.3.2 Blowing synthesis

Inspired by the food “blown sugar”, a blowing synthesis was employed to prepare

strutted graphene.[109] Glucose was mixed with ammonium salts and directly heated to 1350 ºC. The released gases from the decomposition of ammonium salts blew the sugar into strutted graphene. It offered a foam-like structure containing large polyhedral bubbles, with an average diameter of 186 μm. Strutted graphene had a low density of 3.0 mg cm^{-3}, which was comparable to the carbon aerogel. It also possessed a good electric conductivity of 1 S m^{-1} and a high specific surface area of 1005 m^2 g^{-1}, thereby enabling a power density of 893 kW g^{-1} at 100 A g^{-1} in supercapacitor.

3.3.3 3D printing

3D printing refers to the process of connecting or solidifying materials to create 3D objects under the control of computer. Sha et al.[20] reported the synthesis of graphene foam via 3D printing method. Nickel particles with a diameter of 2-3 μm were used as the template and catalyst and sucrose coated on nickel particles was used as the carbon source. A thin layer of powder containing sucrose-coated nickel particles was first set on the platform, followed by laser radiation to produce graphene layers. After first rastering, another thin layer of powder was manually added onto the top, followed by the same laser radiation process. After repeating 20 times and template removal, graphene foam was obtained. The obtained materials owned excellent physical properties, such as a high porosity of 99.3 %, a low density of 15 mg cm^{-3}, a high electrical conductivity of 8.7 S cm^{-1} and remarkable storage modulus of 11 kPa.

3.3.4 Laser scribed patterning

El-Kady et al.[143] first reported the successful synthesis of porous graphene films via a simple all-solid-state approach by laser irradiation. Typically, GO suspension was drop casted onto the commercialized CD drive, followed by thermal reduction by laser irradiation. The originally stacked graphene sheets were well exfoliated in this process and as-obtained porous graphene film displayed excellent conductivity (1738 S/m) and

excellent mechanical flexibilities. This synthetic method was also employed in engineering graphene-based electronic devices with low-cost and commercialization possibilities.[144]

4. Metal-ion storage mechanisms

Graphene is regarded as the promising energy storage materials in various MIB systems, including LIBs, SIBs, potassium-ion batteries (PIBs), and aluminum-ion batteries (AIBs).[24,29,145–147] The metal-ion storage in graphene layers is generally achieved *via* intercalation or/and adsorption, as illustrated in Fig. 5. During charging, metal ions will be intercalated into graphene layers or/and adsorbed onto the graphene surface; for discharging, metal ions will be deintercalated or desorbed from graphene layers. In this chapter, we will illustrate and discuss the metal-ion storage mechanisms of graphene layers in different MIB systems.

4.1 Intercalation sites

4.1.1 Lithium-ion batteries

Lithium ions, with a radius of 76 pm, are able to intercalate into graphitic carbon layers and form lithium-graphite intercalation compounds (Li-GICs), i.e. Li_xC_n.[148] Theoretically, one lithium atom can combine with six carbon host atoms at most in a charging process, according to the Equation 3.

$$x\mathrm{Li}^+ + x\mathrm{e}^- + \mathrm{C_n} \rightarrow \mathrm{Li}_x\mathrm{C_n} \quad (3)$$

Based on theoretical calculations, it was predicted that electrochemical behavior of Li^+ intercalation and deintercalation in graphene layers resembles that of graphite.[149–151] Experimental results further demonstrated this electrochemical behavior. High quality graphitized graphene with very few defects was prepared to study the lithium-ion storage behavior. The observation of cathodic peak below 0.2 V demonstrated the intercalation of lithium ions into graphene layers.[152]

4.1.2 Sodium-ion batteries

Sodium-ion batteries gain lots of attractions for manufacturing large-scale energy storage devices due to the abundance and low cost of sodium resources.[32] However, the large radius of sodium ions (102 pm) hinders its intercalation into graphitic carbon layers. Preliminary studies showed that the sodium-graphite intercalation compounds (Na-GICs) are also thermodynamically unstable, leading to severe volume expansion during sodiation.[27,153] Until recently, the intercalation of solvated sodium ions into graphite in ether-based electrolyte systems was realized, according to the Equation 4.[154] By sodium ions and solvent cointercalation, the graphite anode could deliver a reversible capacity of 150 mAh g^{-1} after 2500 cycles.[155]

$$C_n + e^- + A^+ + y\text{solv} \rightarrow A^+(\text{solv})_y C_n^- \quad (4)$$

Sodium ions can intercalate into graphene layers with large interlayer spacings. Cao et al. [156] studied the theoretical energy cost for sodium-ion insertion as a function of carbon interlayer spacing. They found the energy cost for sodium insertion would drop with increased carbon interlayer spacings. As for few-layered graphene with an interlayer spacing of 0.37 nm, the energy cost for sodium insertion was only 0.053 eV, which was low enough to conquer for sodium insertion. Mechanism studies on sodium-ion storage in hard carbon further demonstrated this theory. Ding et al. [157] studied the sodium-ion storage of carbon nanosheets frameworks, which contained 4-5 stacked surface graphene layers. During sodiation, the interlayer spacing of graphene layers was expanded from 0.396 nm to 0.416 nm at the low voltage below 0.1 V, demonstrating the sodium insertion into graphene layers.

4.1.3 Potassium-ion batteries

Potassium, is considered as a candidate for new MIB systems owing to its

abundance, less complex surface reactions, high ionic conductivity and low redox potential of K/K^+ (-2.92 V *vs.* standard hydrogen electrode). Hu et al.[158] demonstrated that potassium ions can intercalate into the interlayer of graphitic materials by a three-step staging process resembling lithium intercalation: C→KC_{24} (Stage III)→KC_{16} (Stage II)→KC_8 (Stage I). In a typical discharging profile, a relatively flat slope was observed in the voltage range of 0.35 V to 0.18 V, resulting from the formation of KC_{24} in Stage III. A voltage transition at 0.14 V was observed, indicating the formation of KC_{16} in Stage II. The remaining capacity was attributed to the formation of KC_8 in Stage I. By such three-step staging process, graphite displayed an initial intercalation capacity of 270 mAh g^{-1} at 5 mA g^{-1}. The potassium-ion storage in graphene layers (rGO film) was also studied.[29] Different from the potassium-ion storage behavior in graphite, dilute Stage I was formed in the voltage range of 0.37 to 0.24 V, and then a voltage transition from Stage VI at 0.24 V (KC_{72}) to Stage II at 0.15 V (KC_{24}) was observed. The remaining capacity below 0.5 V resulted from the synthesis of Stage I compound (KC_8). As a result, rGO anode exhibited a stable capacity of 140 mA h g^{-1} after 100 cycles at 100 mA g^{-1}. Therefore, it was concluded that potassium ions could be stored in graphene layers through intercalation.

4.1.4 Aluminum-ion batteries

Owing to the abundance, low flammability, and three-electron redox properties of aluminum, aluminum-ion batteries (AIBs) have been extensively studied.[159,160] Graphite was demonstrated to be an ideal material for aluminum-ion intercalation in the ionic liquid ($AlCl_3$/[EMIm]Cl) electrolyte.[161] The aluminum-ion storage mechanisms (Equation 5 and 6) are revealed as follows, where n represents the molar ratio of carbon atoms to intercalated anions in the graphite.

$$4Al_2Cl_7^- + 3e^- \leftrightarrow Al + 7AlCl_4^- \quad (5)$$

$$C_n + AlCl_4^- \leftrightarrow C_n[AlCl_4] + e^- \quad (6)$$

Although breakthrough has been made in the Al/$AlCl_3$-[EMIm]Cl/graphite system,[161] the intercalation and de-intercalation of $AlCl_4^-$ could only penetrate through the edges of graphite with a rather limited penetration path. Aiming to overcome this obstacle, defect-free graphene with more open edges was prepared to facilitate the ion intercalation. Chen et al.[146] reported the preparation of defect-free graphene film with interconnected 3D infiltration channels by high-temperature annealing treatment on rGO film. The porous surface structure facilitated the vertical infiltration of electrolyte, thereby shortening the pathways for the transport of electrolyte ions. Meanwhile, 3D channels also acted as highways for the electron transfer. A substantially enhanced aluminum-ion storage property was observed, exhibiting superior rate performance (120 mA h g^{-1} at 400 mA g^{-1}) and excellent cyclic performance (91.7 % retention after 250000 cycles). It also owned a wide operation temperature in the range of -40 to 120 ^oC and exhibited superior flexibility for wearable applications, with no capacity loss after folding 10000 times. Chen et al.[162] also synthesized high-quality graphene microflower for high-performance AIBs. Graphene microflower cathode exhibited a high capacity of 100 mA h g^{-1} without decay after 5000 cycles at 5 A g^{-1} and a good rate capability with a capacity of 92 mA h g^{-1} at 8 A g^{-1}. In addition, a high energy density of 40 Wh kg^{-1} and a high power density of 3000 W kg^{-1} were achieved. The aluminum-ion storage properties of other reported 3D graphene materials are summarized in Table 2. [50–54]

4.2 Adsorption surface

4.2.1 Lithium-ion batteries

Graphene layers can provide the active surface for lithium-ion adsorption,

displaying efficient lithium storage. In 1995, Dahn et al.[148,163] proposed that both sides of the graphene layer are capable for lithium-ion adsorption. It would theoretically synthesize Li_2C_6 phase and thus exhibited a high capacity of 744 mAh g^{-1}, which is twice as much as traditional graphite. Sonia et al.[164] studied the lithium-ion storage properties of few-layered graphene with very few defects. The discharge profile for few-layered graphene below 0.3 V was fairly similar to that of bulk graphite. However, lithium-storage capacities of few-layered graphene are four times greater than graphite (Fig. 6a-b). To explain the extra capacity of graphene, kinetic behaviors of both electrodes were analyzed by using the power law formula (Equation 7).

$$i = av^b \tag{7}$$

Where $b = 1$ indicated the capacity is provided by surface-controlled adsorption process and $b = 0.5$ indicated the capacity is provided by diffusion-controlled intercalation process. By calculating the b value from the slopes of log (i) *vs.* log (v) plots at different potentials (Fig. 6c-d), the contribution from intercalation and adsorption to the overall capacity can be quantified. It was found that surface-controlled adsorption contributes a lot to the overall capacity, demonstrating graphene layers can serve as the adsorption surface for lithium-ion storage.

Some studies reported graphene with heteroatoms or surface defects exhibited a capacity even exceeding its theoretical value of 744 mAh g^{-1}. For example, sulfur-doped graphene with 3D cellular architecture displayed a reversible capacity of 1697 mA h g^{-1} at 0.1 A g^{-1}.[55] The extra capacity needs further explanation. Many in-depth investigations were made to understand this abnormal storage behavior.[165–167] First principle calculation demonstrated that structural defects in graphene layers can bind with Li^+ stably, offering extra lithium-ion storage capacity.[165] In addition, Li atom is

energetically favorable to adsorb on various defects, whereas for non-defective graphene, lithium atom could only situate at the hollow sites of hexagonal ring, forming LiC_6.[166] By using in situ transmission electron microscopy (TEM) characterization, the adsorption of lithium ions on defect sites was directly observed.[166]

The lithium storage behavior of graphene edge, as a special form of defective structure, was studied recently.[167] It was found that lithium storage capacity and lithium-ion diffusion ability at graphene edge sites were dramatically enhanced. Chananate et al.[168] demonstrated that the energy barriers at graphene edge sites for lithium diffusion were 0.15 eV lower at most than those of the basal plane of graphene. In addition, lithium-ion diffusion coefficient at graphene edge sites was 2 orders of magnitude higher than planar graphene surface. Very recently, the excess capacity of graphene layers was further interpreted,[164] as shown in Fig. 6f. In a typical lithiation process, lithium ions would first adsorb at the edge sites. Then, with the increase of lithium concentration, lithium ions started to move toward the center, distributing on the entire surface of graphene. After improving the lithium concentration to a certain extent, additional lithium ions could adsorb on the graphene surface, disrupting its original LiC_6 configuration and forming more than one lithium layer.

4.2.2 Sodium-ion batteries

Graphene layers can also offer the active surface for sodium-ion adsorption. Bai et al.[169] obtained misaligned surface graphene layers on hard carbon by carbonizing sucrose at high temperature to study their sodium storage mechanisms. For the hard carbon obtained at 1000 ºC, it exhibited a sloping capacity of 123.1 mAh g^{-1} in the voltage range of 1.2 V to 0.1 V. For the hard carbon obtained at 2000 ºC, the sloping capacity was decreased to 48.8 mAh g^{-1}. The decreased sloping capacity resulted from the evolution of hard carbon structures including surface graphene layers during

carbonization. With the carbonization temperature increases, the amounts of defects and surface functional groups on graphene layers dramatically decreased. Therefore, the adsorption effect of sodium ions on graphene layers with defects or functional groups was demonstrated. Li et al.[170] further confirmed the sodium adsorption on isolated graphene layers. No shift of (002) peaks in in-situ XRD patterns (Fig. 7a) during charge and discharge demonstrated that sodium storage could not be assigned to sodium intercalation but sodium adsorption. In addition, ex-situ XPS spectra of the C1s and Na 1s (Fig. 7b-c) showed a shift to higher energy in plateau-voltage region below 0.12 V, which was attributed to the nanovoids filling. Young Soo Yun et al.[171] demonstrated that sodium-ion adsorption could occur at defective sites on the basal plane of graphene with defects or N-substitution. Various structural defects could contribute to sodium-ion storage containing the following types: carbon vacancies (type 1), carbon divacancies (types 2, 3 and 4), carbon site changes (type 5), and adatoms (type 6) (Fig. 7d). The corresponding chemisorption energy of defect sites was also given (Fig. 7e). They also studied the sodium-ion storage behavior of graphene layers by carbonizing pyroprotein. It was observed that sodium ions were adsorbed on the disordered graphene layers, forming metallic sodium (Fig. 7f-g). Bommier et al.[172] proposed a "three stage" mechanism for sodium-ion storage in nongraphitizable carbon based on computational calculations. In the first stage at the sloping voltage region, sodium ions would adsorb at defective sites on the surface graphene layers; in the second stage at the plateau voltage region, sodium ions would intercalate into graphene layers; In the last stage at the end of plateau voltage region, sodium ions would fill into nanopores.

4.2.3 Potassium-ion batteries

Heteroatoms doped or defective graphene layers are also able to store potassium ions via surface adsorption.[29,173–175] Potassium storage properties of boron doped

graphene were studied by first principle calculations.[29] It was found that carbon atoms substituted by boron atoms resulted in an electron deficiency. Such deficiency of electron distribution led to an enhancement of potassium-ion adsorption at boron doped sites. Theoretically, boron doped graphene could exhibit a high capacity of 546 mAh g^{-1}, forming B_4C_{28}. In addition, boron doped graphene could also improve the safety of PIBs by preventing dendrite growth. Graphene with nitrogen dopants showed similar adsorption effect.[174] Pyridinic nitrogen could also lead to a local electron deficiency and produce affinity to the electron nearby K atom. Therefore, such defect sites on graphene layers could enhance potassium-ion storage properties. In addition, chemical dopants also enlarged the interlayer spacing of graphene layers, which facilitated the insertion and desertion of K^+ ions. Fluorine doped graphene also showed superior potassium-ion storage properties, which was also attributed to the additional potassium bonding sites around the vicinity of fluorine atoms on graphene layers.[175]

5 Secondary metal-ion battery applications

3D graphene materials with structural functionalities play significant roles in fabricating composite electrodes. Aiming to develop advanced MIB systems, these functionalities should be well understood. In this chapter, we classify the functionalities of 3D graphene materials as supporting materials and encapsulating materials to discuss their roles and applications in MIB systems.

5.1 Supporting materials

3D graphene with high electric conductivity, structural superiorities like interconnected and porous network, and excellent mechanical properties like flexibility and robustness, can act as supporting materials to fabricate 3D graphene-based composites. Specifically, in fabricating graphene-based electrodes with other metal-host materials for MIB applications, the 3D architectures of graphene own the following

unique functions: (i) Metal-host materials can be effectively loaded and fixed on the graphene sheets. The aggregation effect of metal-host materials with nanoparticles or layered structures can be suppressed. (ii) The interconnected conductive network of 3D graphene could enhance the electron transfer and abundant pores inside the structure could facilitate the infiltration of electrolyte and shorten the metal-ion diffusion pathways. (iii) Graphene sheets with flexibility can mitigate the volume expansion of the loading metal-host materials.[136,176]

5.1.1 Lithium-ion batteries

Alloy materials (Si,[25,177–181] Ge,[182–188]), metal oxides (TiO_2,[189] SnO_2,[190–192] Fe_2O_3[193]), metal sulfides (MoS_2, [194,195] SnS_2, [196,197] SnS[198]), and $Li_4Ti_5O_{12}$[199] are all belonging to the new class of anode materials for LIB applications. By fabricating 3D graphene-based composites, some issues of these anode materials such as poor electron transfer and structural degradation can be inhibited. Silicon is a promising anode candidate due to its high theoretical capacities (4200 mA h g^{-1}) but suffering from its poor conductivity and large volume expansion (400 %) during lithiation.[25,182–186,200] 3D graphene materials could tackle this problem by serving as the conductive supporting materials. Harold et al.[25] successfully prevented the pulverization of silicon by fabricating silicon@graphene composite. It was prepared by dispersing silicon nanoparticles in GO solution, followed by thermal reduction. Silicon nanoparticles with a diameter in the range of 20-50 nm were well dispersed on the graphene sheets, forming a sandwiched structure. The graphene-based composite electrodes exhibited a capacity of more than 1500 mA h g^{-1} after 200 cycles at 1 A g^{-1} in LIBs. Similar approach was used to synthesize graphene-based composites such as Ge nanoparticles@graphene and Sn nanoparticles@graphene, presenting enhanced lithium storage properties.[182–186,200] Metal sulfides with layered structure show high theoretical

capacity, such as MoS_2 (670 mA h g^{-1}), SnS_2 (645 mA h g^{-1}), SnS (728 mA h g^{-1}), however, they suffered from low conductivity or/and volume change during lithiation.[194–196] Among them, MoS_2 showed minimal volume expansion (103%) during lithiation, showing superiorities compared to other metal sulfides. In order to improve its conductivity, MoS_2 with honeycomb-like nanoarchitectures anchored on 3D graphene foam was prepared by P123-assisted solution-phase method.[194] The obtained material possessed a high specific surface area (182 m^2 g^{-1}), which provided sufficient interface for reactions. The 3D graphene/MoS_2 composite displayed a high discharge capacity (1235.3 mA h g^{-1}) at a low current density of 0.2 A g^{-1} after 60 cycle. Other metal sulfide/graphene composites were also successfully prepared. For example, SnS_2/graphene composite was prepared via hydrothermal method.[196] Different from pure SnS_2 suffering from a rapid loss of capacity in preliminary cycles, SnS_2/graphene composite anodes exhibited an increasing capacity at 0.1 A g^{-1} in first 30 cycles and a stable capacity of 920 mA h g^{-1} after 50 cycles. In addition, good rate capability with a capacity of 600 mA h g^{-1} at 1 A g^{-1} was also obtained.

Metal oxides show similar merits and drawbacks in lithium-ion storage as metal sulfide. 3D graphene supported metal oxide composites have been well summarized and discussed in several reviews, showing great enhancement in cyclic stability compared to pure metal oxides anodes.[26,46,201] $Li_4Ti_5O_{12}$ (LTO) was regarded as promising anode material for LIB applications recently.[202] It owned the merits of no structural changes during intercalation and de-intercalation of lithium ions and high voltage plateau (1.5 V *vs*. Li^+/Li) preventing the formation of lithium dendrite. However, its low lithium-ion diffusion efficiency (10^{-9} to 10^{-16} cm^2 s^{-1}) and poor electric conductivity lead to a poor rate capability for LIB applications. Base on this concern, 3D graphene foam/LTO was prepared to enhance the transport of lithium ions and

electrons. As a result, 3D graphene foam/LTO anodes presented excellent rate performance with a capacity of 135 mA h g^{-1} at 200 C (1 C=145 mA h g^{-1}).[199]

Cathode materials, including metal oxide composites,[203,204] phosphate,[99,199] silicate[99,205] and organic polymer,[206,207] were also composited with 3D graphene materials to enhance their lithium storage properties. $LiMPO_4$ (M represents Fe, Co, Ni and Mn), with a typical olivine structure, gains attractions as cathode material in LIBs. Typically, $LiFePO_4$ (LFP) has realized industrialization in electric vehicles due to its stable discharge voltage plateau, thermal stability and chemical stability. However, it still suffers from poor conductivity and sluggish ion diffusion. Cheng et al. [199] first reported a flexible full battery using LTO/graphene foam as anode and LFP/graphene foam as cathode. It presented a good rate capability with a capacity of 117 mA h g^{-1} at 10 C for 100 cycles, as shown in Fig. 8a-b. $Li_3V_2(PO_4)_3$ (LVP) is also a very promising candidate due to its high theoretical capacity (197 mA h g^{-1}) and a high average voltage of 4 V during cycling. Its intrinsic poor conductivity can be improved by fabricating 3D graphene/$Li_3V_2(PO_4)_3$ composites. Liu et al.[208] demonstrated the transport of lithium ions in LIBs can be enhanced by preparing $Li_3V_2(PO_4)_3$@graphene composite. It showed excellent rate performance with a capacity of 47 mA h g^{-1} after 1000 cycles at 50 C. Very recently, $LiNi_{0.6}Co_{0.1}Mn_{0.3}O_2$ (NCM)/graphene balls composite was also prepared.[209] Graphene balls were grown on the SiO_2 particles via CVD method, followed by coating on NCM via ball milling. SiO_2 played a dominant role in ball milling, which facilitated the penetration of graphene balls into spaces between pristine NCM (Fig. 8c-i). Graphene balls, with a minimal content of 0.425 wt%, could substantially enhance the lithium storage properties. The composite cathodes presented much improved energy density (27.6%) compared to traditional NCM material. In addition, good cyclic performance was demonstrated at different temperatures (25 ºC

and 60 ºC), as shown in Fig. 8j.

Metal oxide composites like $LiMn_2O_4$ (LMO), $LiNi_{1-x-y}Co_xMn_yO_2$ (NCM) have been investigated extensively as cathodes in LIBs. LMO owns the merits including low cost, non-toxicity and safety, but poor conductivity (10^{-6} S cm^{-1}) and the dissolution of Mn^{2+} in electrolyte limit its practical use.[203] Bak et al.[203] reported the fabrication of spinel $LiMn_2O_4$/rGO composite via a chemical route. Well dispersed LMO particles on rGO sheets exhibited a high capacity of 137 mA h g^{-1} at 1 C and an improved rate capability with a capacity of 101 mA h g^{-1} at 100 C. NCM is also commercialized cathode material due to its high energy density, stable structure and low cost. However, it faces the issues of poor rate capability owing to the cation disorder during the thermal treatment, where lithium ions could detach from its original sites, leading to limitation in kinetics. In this regard, Jiang et al.[210] reported the synthesis of reduced GO networks/$LiNi_{1/3}Co_{1/3}Mn_{1/3}O_2$ composite as cathode material in LIBs. By anchoring NCM materials on rGO network, the ion diffusion pathways were shortened, thus improving the ion diffusion kinetics. The Nyquist plots demonstrated that the charge transfer resistance of rGO/$LiNi_{1/3}Co_{1/3}Mn_{1/3}O_2$ composite was significantly reduced. As a result, the composite cathode exhibited a capacity of 55 mA h g^{-1} at 20 C (1 C = 170 mA g^{-1}). In comparison, pure $LiNi_{1/3}Co_{1/3}Mn_{1/3}O_2$ showed almost no capacity at 20 C.

Li_2MSiO_4 (M represents Mn, Fe, Co, Ni) possess high theoretical capacity, low cost and thermal stability. The main obstacles to achieve its practical application are amorphization and Jahn-Teller distortion of Li_2MSiO_4 during lithiation, resulting in severe volume change. 3D graphene/Li_2MSiO_4 composites could inhibit the volume change, thereby enabling better lithium-ion storage properties.[99,205] For instance, graphene-based Li_2FeSiO_4 composite cathode for LIBs was constructed, which

exhibited a high capacity of 313 mA h g^{-1} in initial discharge, 93% of its theoretical capacity (333 mA h g^{-1}).[99] In addition, a capacity of 45 mA h g^{-1} was obtained even at a high rate of 50 C (1 C = 166 mA g^{-1}).

Organic polymers, such as organic sulfur compounds,[44] carbonyl compounds,[206,207] and conducting polymer,[159] also show promises as cathode materials due to its high theoretical capacities and fast reaction kinetics. However, intrinsic insulation properties and dissolution of organic polymers in organic electrolyte hurdle their practical applications. Huang et al.[211] fabricated 3D graphene/PI composite by in-situ polymerization of PI particles on the graphene surface. The composite showed an enhanced conductivity of 2.38 S cm^{-1} and improved charge transfer due to the strong coupling between graphene and PI particles. The composite cathodes exhibited a high reversible capacity (240 mA h g^{-1} at 0.04 A g^{-1}) and good rate performance (102 mA h g^{-1} at 40 A g^{-1}).

5.1.2 Sodium-ion batteries

Promising sodium-host anode materials include metal oxides,[212–214] metal sulfide,[215] phosphide,[135,216–218] and $Na_2Ti_3O_7$.[219] Metal oxides, SnO_2 for example, owned a high theoretical capacity (1398 mA h g^{-1}) but pure SnO_2 anode displayed a rapid capacity loss owing to severe volume expansion during sodiation.[220,221] In this regard, Patra et al.[212] reported the preparation of SnO_2 particles on graphene sheets by hydrothermal method with the existence of supercritical state CO_2. Supercritical state CO_2 could assist the uniform dispersion of SnO_2 particles on graphene sheets owing to their near-zero surface tension. In addition, excellent penetration ability could also facilitate the mixing between graphene and SnO_2 particles. As a result, 3D graphene/SnO_2 displayed a reversible capacity of 400 mA h g^{-1} at 20 mA g^{-1}, a high rate capability of 207 mA h g^{-1} at 10 A g^{-1} and also good cyclic performance with 82%

retention after 100 cycles. Su et al.[213] also reported the SnO_2 anchoring on graphene as anode materials, which exhibited a high reversible capacity over 700 mA h g^{-1} after 100 cycles. Other metal oxides (Fe_3O_4,[214] Co_3O_4,[222] MoO_3,[223] Sb_2O_3[224]) have been also composited with 3D graphene materials, showing enhancements in sodium-ion storage properties.

Layered transitional metal sulfides own the structural superiority of large interlayer spacing for the accommodation of sodium ions. For example, MoS_2 owns a larger interlayer spacing (0.62 nm) compared to graphite (0.33 nm), which facilitates the intercalation of sodium ions. However, Layered MoS_2 can easily restack with each other due to its large surface energy, resulting in the loss of active surface area. Choi et al.[215] synthesized MoS_2-graphene spheres composite by one-pot spray pyrolysis. The uniform graphene nanospheres suppressed the stacking of MoS_2 layers, thereby lowering the barrier for Na^+ intercalation. The composites displayed a capacity of 322 mA h g^{-1} at 1.5 A g^{-1} after 600 cycles. Similarly, SnS_2 layers also own sandwiched structures with large interlayer spacing (0.59 nm), which is prone for sodium intercalation. Exfoliated SnS_2 anchored on graphene sheets was prepared to enhance the sodium storage.[225] SnS_2 nanoplates containing 2-5 layers were uniformly decorated on the surface of graphene by hydrolysis of lithiated SnS_2, followed by hydrothermal treatment. It exhibited a high capacity of 610 mA h g^{-1} after 300 cycles and performed a high rate capability with a capacity of 326 mA h g^{-1} at 40 A g^{-1}. Apart from SnS_2, SnS nanoparticles anchored on nitrogen-doped graphene was also prepared, exhibiting a high capacity of 509.9 mA h g^{-1} at 2 A g^{-1} after 1000 cycles.[226]

Phosphides own the merits of high theoretical capacities and low redox voltages as anode materials in SIBs.[135,216–218] However, they suffer from low intrinsic electric conductivity and volume expansion during sodiation.[217] In this regard, Wu et

al.[216] reported the preparation of graphene/Ni_2P composite via a template-assisted self-assembly method. 3D yolk-shell-like Ni_2P nanoparticles were successfully embedded into porous graphene networks. The graphene/Ni_2P hybrid anodes reached a capacity of 161 mA h g^{-1} at 0.2 A g^{-1} after 100 cycles. Sn_3P_4, combining good conductivity of Sn and high capacity of P, displays high theoretical volumetric capacity (6650 mAh cm^{-3}), high conductivity (30.7 S cm^{-1}) and gravimetric capacity of 1132 mAh g^{-1} as promising anodes in SIBs. Micro-sized Sn_3P_4 particles could be prepared by mechanical ball milling method, however, they had to face the pulverization issue during sodiation.[227] Nano-sized Sn_3P_4 particles would suppress the pulverization effect, but they suffer from the particle aggregation. In this regard, uniformly monodispersed Sn_3P_4 nanoparticles loaded on rGO sheets were prepared by an in-situ low temperature solution-based phosphorization chemical transformation route. Since pulverization and aggregation of the particles are depressed, the composite anodes delivered a high capacity of 362 mA h g^{-1} after 1500 cycles at 1 A g^{-1}.[135] Other graphene-based composites such as 3D graphene/$Na_2Ti_3O_7$ nanowires,[219] 3D graphene/Sn,[228] 3D graphene/$NaTi_2(PO_4)_3$,[229] and 3D graphene/$MoSe_2$[230] have also been synthesized, presenting enhanced sodium-ion storage properties.

Tremendous advancements have been made in developing cathode materials for SIB applications, including polyanion-based material and organic polymer. Polyanion materials with 3D structure and large interstitial lattice enable fast sodium-ion diffusion kinetics as anodes in SIBs. Among them, $Na_3V_2(PO_4)_3$ (NVP) with NASICON-type framework (Fig. 9a), gains lots of attractions as anodes in SIBs owing to its high thermal stability, high operating voltage (3.4 V *vs*. Na/Na^+) and rapid ionic mobility (exceeding 10^{-11} cm^2 s^{-1}). However, limitation still resides in its poor conductivity.[145,231,232] In this regard, Fang et al.[232] reported the fabrication of carbon NVP particles with carbon-

coating layer embedded in 3D graphene network. Through double restrictions of carbon layers and graphene network, the structure of NVP particles can be well maintained (Fig. 9b-e). In addition, the incorporation of graphene network also released the strain caused by volume changes of NVP particles during sodiation. As a result, the composite electrodes exhibited a capacity of 97.2 mA h g^{-1} at 10 C and a good cyclic performance with 82 % capacity retention for 1500 cycles at 40 C (Fig. 9f-g). Recently, carbon coated NVP nanocrystals wrapped by rGO sheets was successfully prepared.[233] The composite cathode could achieve superior sodium storage properties due to the rapid Na^+ and electron transports. It displayed a high reversible capacity of 115 mA h g^{-1} at 1 C, a high rate performance with a capacity of 86 mA h g^{-1} at 100 C, a high energy density of 384 W h kg^{-1} at a low specific power of 0.4 kW kg^{-1} and also a good cyclic performance with 64 % retention after 10000 cycles. The sodium-ion storage properties of sodium vanadium fluorophosphates were also studied.[234,235] $Na_3V_2O_2(PO_4)_2F$/carbon/graphene composite was successfully synthesized as cathode in SIBs. 3D graphene with nanoporous structure could facilitate the electrolyte infiltration, thereby shortening the Na^+ transport pathways. [234] As a result, the composite cathode exhibited a capacity of 135.8 mA h g^{-1} at 0.1 C and cyclic stability with a capacity retention of 96.8% at 2 C after 50 cycles. Jin et al.[235] also reported the preparation of $Na_3V_2O_2(PO_4)_2F$ nanocubes/C/graphene composite, which delivered a reversible capacity of 113.2 mA h g^{-1} at 1 C.

$Na_7V_4(P_2O_7)_4(PO_4)$ is a type of mixed-polyanion materials containing multiple intercalation sites for sodium-ion storage (Fig. 9h). Its practical application is limited by sluggish electron transfer. 3D graphene-based composite cathodes were constructed to improve the low conductivity of $Na_7V_4(P_2O_7)_4(PO_4)$. Zhang et al.[236] fabricated the $Na_7V_4(P_2O_7)_4(PO_4)$/C nanorod-graphene composite by a molten-salt synthetic strategy

(Fig. 9i-j). The conductivity of graphene-based composite (0.76 S cm^{-1} at 65 °C) was dramatically enhanced compared to pristine $Na_7V_4(P_2O_7)_4(PO_4)$/C nanorod composite (5.41×10^{-3} S cm^{-1} at 65 °C). As a result, $Na_7V_4(P_2O_7)_4(PO_4)$/C nanorod-graphene composite exhibited an enhanced rate performance and a good cyclic performance with 95 % retention after 200 cycles at 1 C, as shown in Fig. 9k-l.

Organic polymers have significant merits including high theoretical capacity and low cost but suffering from electrical insulation for SIB applications. Constructing graphene-based composite electrodes is a promising approach to solve this issue. Huang et al.[211] reported the preparation of 3D graphene/PI composite for sodium ion storage. It displayed a capacity of 213 mA h g^{-1} at 0.05 A g^{-1} and a good cyclic performance with 80% capacity retention after 1000 cycles. Poly (anthraquinonyl sulfide) (PAQS), with a high theoretical capacity of 225 mA h g^{-1} and insoluble properties in any solvents, is regarded as the promising cathode material for SIBs. Zhang et al.[237] reported the successful preparation of 3D graphene/PAQS composite via a dispersion-assembly strategy. Compared to pristine PAQS particles with severe aggregation, PAQS particles in 3D graphene composite have a decreased particle size in the range of 100 to 200 nm. The composite cathode delivered a reversible capacity of 156 mA h g^{-1} at 0.1 C (1 C = 225 mA h g^{-1}) and a capacity of 132 mA h g^{-1} at 0.5 C with 84.1% capacity retention after 1000 cycles.

5.1.3 Aluminum-ion batteries

Metal sulfides with large interlayer spacings can serve as intercalation sites for aluminum-ion storage. For example, SnS_2 with a lamellar structure and a large interlayer spacing (0.59 nm) can facilitate the intercalation and deintercalation of large $AlCl_4^-$ (about 0.53 nm). However, bulk SnS_2 material has a less porous structure for electrolyte infiltration, resulting in sluggish aluminum-ion diffusion kinetics.[196] In view

of this concern, SnS_2 nanosheets@rGO network was successfully synthesized.[51] SnS_2 nanosheets were evenly distributed on the surface of rGO, enabling increased active sites for aluminum-ion insertion. In addition, porous structure of rGO network also accelerate the ion transport. The composite cathode displayed a high energy density of 241 Wh kg^{-1} and a good rate capability with a capacity of 112 mA h g^{-1} at 10 A g^{-1}. Recently, a novel cathode material, Ni_3S_2/graphene composite, was prepared for AIB application.[50] Graphene sheets could serve as highly conductive channels to reduce intrinsic resistance of the composite cathode. The composite cathode exhibited high discharge voltage plateau (~1.0 V *vs*. Al/$AlCl_4^-$) and a discharge capacity of over 60 mA h g^{-1} after 100 cycles at 100 mA g^{-1}.

5.1.4 Potassium-ion batteries

Metal sulfides with large interlayer spacings can also serve as intercalation sites for potassium-ion storage. Constructing 3D graphene-based composite electrodes can further enhance their potassium-ion storage properties.[238,239] For example, a novel PIB anode containing SnS_2/rGO network was constructed, exhibiting a high capacity of 250 mA h g^{-1} after 30 cycles.[238] Sb_2S_3 nanoparticles embedded in the graphene framework was also prepared, displaying an energy density of 166.3 W h kg^{-1} as anode in a full PIB.[239] CoS quantum dots@graphene composite with large surface area, high conductivity and robust structural stability was successfully synthesized.[240] It displayed a high capacity of 310.8 mAh g^{-1} after 100 cycles as the PIB anode. In comparison, pure CoS anode only exhibited a capacity of 126.3 mA h g^{-1} after 60 cycles. In another study, MoS_2 with a flower-like structure was grown on rGO sheets via a solvothermal method.[241] It exhibited a high reversible capacity of 381 mA h g^{-1} after 100 cycles as the PIB anode. Other applications of 3D graphene as supporting materials in PIBs are summarized in Table 2. [173–175,238–241]

5.1.5 Magnesium-ion batteries

Magnesium is a desirous anode material owing to its abundance in the earth crust and the high volumetric energy density of 3837 mA h cm^{-3}. In view of this, magnesium-ion battery system was explored.[242] Till now, sluggish reaction kinetics in cathodes, derived from the strong polarizing effect of divalent Mg ions, hinders the development of Mg-ion batteries. For example, V_2O_5, as cathode in Mg-ion batteries, suffered from a rapid capacity loss in the first 7 cycles.[243] This is attributed to the sluggish reaction kinetics of Mg-ion intercalation and poor electrical conductivity of V_2O_5 cathode. 3D graphene and V_2O_5 composite was prepared to ameliorate this situation.[244] Graphene decorated vanadium oxide nanowire aerogel was successfully prepared. The diffusion coefficient of Mg ions in cathode was improved (~3 x 10^{-11} cm^2 s^{-1}), resulting in an enhanced rate capability. The composite cathode exhibited a capacity of 320 mA h g^{-1} at 50 mA g^{-1}. Moreover, it had a good cyclic performance with 81 % capacity retention after 200 cycles at 1 A g^{-1}. In addition, magnesium-ion batteries also showed a wide temperature range of operation, with a capacity of over 200 mA h g^{-1} (> 55 ^oC) and a reversible capacity of 40 mA h g^{-1} (- 30 ^oC). Other promising electrode materials like nanowire Mg-OMS-2, Co_3O_4, MoS_2, $FeVO_4$ were also anchored on 3D graphene materials, showing enhanced Mg-ion storage properties, which are summarized in Table 2.[147,245–247]

5.2 Encapsulating materials

3D graphene is increasingly playing the role of encapsulation in constructing the graphene/metal-host material composite electrodes. Encapsulation of metal-host materials can be achieved either by self-assembly of graphene sheets or by template-assisted growth of graphene sheets. The particularities and superiorities of 3D graphene as encapsulating materials can be summarized as follows. Firstly, rationally designed

void space in the composite electrodes can be used to accommodate the volume expansion of metal-host materials. Secondly, the strains caused by volume changes of metal-host materials can be released due to the flexibility and mechanical robustness of graphene sheets. Thirdly, owing to the encapsulation effect of graphene, the pulverized metal-host materials cannot scatter into the electrolyte, thus preserving the electrical contact of metal-host material. Lastly, stable SEI film can be formed on the surface of graphene, thereby preventing the side reactions.

5.2.1 Lithium-ion batteries

Metal oxides and alloys were encapsulated into 3D graphene materials to enhance their lithium-ion storage properties. For instance, MnO nanowires encapsulated in tubular graphene scrolls was prepared by hydrothermal method, forming a core-sheath structure.[248] The graphene scrolls were electronically connected with the MnO nanowires but mechanically isolated, leaving void spaces. In this way, graphene scrolls could enhance the electric conductivity as well as accommodate the volume expansion of metal oxides during lithiation. As a result, it displayed excellent storage and cyclic properties, with a capacity of 812 mA h g^{-1} at 2 A g^{-1} after 1000 cycles. In addition, 3D graphene encapsulating SnO_2 hollow spheres was also prepared.[249] As the composite anode in LIBs, a capacity of 552 mA h g^{-1} at 1 A g^{-1} was observed after 500 cycles, presenting remarkable enhancements compared to pure SnO_2 anode. Recently, graphene cage encapsulating SnO_2 with optimized size of the void space was constructed.[106] The volume of the void space perfectly matched the expanded volume of tin oxide (~260%) after lithiation. The resultant material exhibited high volumetric energy density (2123 mA h cm^{-3}) and high reversible capacity (974 mA h g^{-1}). Xu et al.[184] reported the preparation of graphene encapsulating germanium nanowires by CVD method. Graphene shells with high flexibility could provide mechanical tight

holding of Ge. Meanwhile, their high conductivity could also accelerate the transmission of electrons. The composite anode exhibited a high capacity of 1400 mA h g^{-1} at 1 C (1 C = 1600 mA g^{-1}). Even at a high current density of 20 C, a capacity of 517 mA h g^{-1} was still maintained.

3D graphene encapsulating cathode materials were also reported for LIB applications. The synthesis of Aminoanthraquinone (AQ) nanowires encapsulated in 3D graphene framework was reported.[207] 3D graphene framework could suppress the dissolution of AQ in electrolyte by encapsulation. As a result, the composite cathode exhibited good cyclic stability with a capacity retention of 76% after 1000 cycles. V_2O_5 as a promising cathode material in LIBs suffered from low conductivity (10^{-2}-10^{-3} S cm^{-1}) and low lithium-ion diffusion coefficient (10^{-12}-10^{-13} cm^2 s^{-1}).[250–252] In this regard, crumple rGO encapsulated hollow V_2O_5 microsphere was prepared.[253] The encapsulating crumple rGO could prevent the dissolution of vanadium ions into electrolyte and improve electrolyte wettability of the composite cathode. The composite cathode offered a high energy density of 492 W h kg^{-1}, a high capacity of 289 mA h g^{-1} at 0.1 A g^{-1}, and a high rate capability with a capacity of 163 mA h g^{-1} at 5 A g^{-1}. In addition, capacity retention of 94% was obtained after 200 cycles at 2 A g^{-1}.

5.2.2 Sodium-ion batteries

Phosphorus is a promising anode material in SIBs with a high theoretical capacity of 2596 mA h g^{-1}. However, it suffers from insulating electronic nature (1 x 10^{-14} S cm^{-1}) and volume expansion (300 %) during sodiation.[254] In this consideration, the rGO encapsulated phosphorus/carbon composite was successfully prepared by a simple spray drying process.[255] As a result, the composite anodes displayed a high reversible capacity of 2445 mA h g^{-1} and an improved cyclic stability with a capacity retention of 95 % after 100 cycles. Other novel anode materials in SIBs including VO_2[256] and

$NiCo_2O_4$[257] were also encapsulated by 3D graphene materials, showing enhanced sodium-ion storage capabilities. LTO is considered as high safety anode in SIBs due to its high operating voltage (0.9 V), which can prevent the formation of sodium dendrite. In addition, it also offers an adequate theoretical capacity of 175 mA h g^{-1}. The major obstacles to achieve its practical applications in SIBs are its intrinsic low ionic and electronic conductivity. In this consideration, porous LTO nanofibers aerogel wrapped by graphene sheets was prepared.[258] A stable SEI film was formed on the graphene, thereby enabling the durability of SIBs. The composite anodes exhibited a high capacity of 195 mA h g^{-1} and superior cyclic performance up to 12000 cycles in SIBs.

As for cathode materials in SIBs, $Na_3V_2O_2(PO_4)_2F$ shows promises due to its high reversible capacity (~ 130 mA h g^{-1}) and high average discharge voltage (~ 3.8 V *vs*. Na^+/Na). However, its poor conductivity limits practical use. In view of this, $Na_3V_2O_2(PO_4)_2F$ nanoparticles were encapsulated in 3D graphene skeleton by a spray drying method.[259] The composite cathode exhibited a high specific capacity of 127.2 mA h g^{-1}, an excellent rate capability with a capacity of 70.3 mA h g^{-1} at 100 C and a long cycling stability with 83.4 % capacity retention over 2000 cycles. In addition, graphene encapsulated NVP was also prepared, showing a reversible capacity of 115.2 mA h g^{-1} at 0.2 C and 70.1 mA h g^{-1} at 30 C.[260]

6. Merits and drawbacks

The applications of 3D graphene architectures in MIB systems own merits and drawbacks. In this chapter, we discuss the strengths and weaknesses of different 3D architectures for MIB applications both in metal-ion storage and in fabricating composite electrodes.

CGBs self-assembled from GO sheets, despite their mass production capability and aggregation-resistant property, generally possess ill-defined molecular structures

and porosity. Defects and oxygen-containing groups of CGBs result in much decreased electron mobility compared to defect-free graphene, and meanwhile, the polydispersity of pore sizes led to inhomogeneities in electrodes. These shortages hinder their applications in metal-ion storage.[261] In comparison with CGBs, GBs prepared by CVD method present well-defined pore structures and the better crystallinity, enabling structural homogeneities and effective metal-ion storage with enhanced electron transfer.[12,106] In addition, GBs can serve as encapsulating materials in fabricating composite electrodes, which owns many configuration superiorities.

3D graphene with linear secondary structures exhibit inferior metal-ion storage properties due to their sparse storage sites. For example, graphene fibers, with stacked graphene sheets forming compact structures, are not promising for metal-ion storage since metal ions hardly intercalate into the interlayer of graphene fibers. Graphene tubes and graphene scrolls containing less stacked graphene sheets also show relatively poor metal-ion storage capabilities because intercalation will primarily occur on the edges of tubes/scrolls at both ends.[75,77] For the preparation of composite electrodes, graphene scrolls can encapsulate metal-host materials by forming core-sheath structures, thereby enhancing the sodium-ion storage properties.[248]

VGS with exposed edges present many unique advantages in metal-ion storage. For example, the lithium-ion diffusion at edge sites can be accelerated, thus enhancing the rate capabilities of LIBs.[168] Meanwhile, graphene edges can also act as adsorption interface to store a large amounts of metal ions via covalent interactions, forming metallic layers such as lithium layers or sodium layers.[164,171]

3D graphene networks are numerously reported as anode materials for metal-ion storage. Their interconnected networks enhance the electron transport and their highly porous structures facilitate the electrolyte infiltration and reduce the ion diffusion

path.[262] Despite these characteristics, their ascendancy is mainly reflected in fabricating graphene-based composite electrodes.[5] 3D graphene networks prepared by self-assembly method own abundant surface functional groups, which provides opportunities for synthesizing composite materials due to the binding effect between the functional groups and other species. 3D graphene networks prepared by CVD method offer well-defined structures, which can act as the scaffold to uniformly load other metal-host materials. It should be noted that the loading materials may be detached from graphene networks during metal-ion intercalation, caused by the volume expansion and weak binding forces between two phases.

The merits of graphene cages are reflected in fabricating graphene-based composite electrodes. Graphene cages can buffer or accommodate the volume expansion of metal-host materials to suppress the structural degradation of electrodes. In addition, in-situ formation of graphene cages on metal-host materials ensures a mechanical tight holding of metal-host materials, generating an encapsulation effect. Such effect will alleviate the pulverization problem of the metal-host materials, thereby improving the stability of composite electrodes.[43]

7. Summary and outlook

3D graphene materials, with superior physicochemical properties, have received so much attention in these years. In this review, we comprehensively summarize the configurations and preparations of 3D graphene materials and specify their applications in MIBs. Basically, two preparation methods, i.e. CVD and self-assembly, are used to construct various 3D graphene architectures, showing promises for energy and environmental applications. In particular, the applications of 3D graphene materials in MIB systems exhibit attractive metal-ion storage properties in many aspects, such as gravimetric energy densities, power densities and cyclic performance. We further reveal

the reasons of these properties by illustrating metal-ion storage mechanisms in graphene layers and by discussing the functionalities of 3D graphene architectures. Last, merits and drawbacks of applying different 3D graphene architectures in MIB systems are also discussed in detail.

Although promising, there are still some remaining challenges that hinder the application of 3D graphene materials in MIBs. As for preparations, self-assembly method shows potential for mass production of 3D graphene materials, however, the resultant materials possess inferior quality caused by defects and oxygen-containing groups. Extra annealing treatment is required to improve the quality of the products. The resultant materials also have ill-defined pore structures, leading to structural inhomogeneities in electrodes, thereby causing highly non-reproducible performance of MIBs. CVD method is capable to obtain high-quality graphene and precisely control the pore structures, however, harsh conditions such as high temperatures and low pressures limit the possibility of large-scale preparation.

As regards the 3D graphene-based composite electrodes for MIB applications, some crucial issues need to be addressed. First, poor initial columbic efficiency makes composite electrodes unfeasible, since additional quantities of electrode materials are required to supply the first charge. Second, complex electrochemical reactions between graphene layers and metal ions often results in the capacity fluctuation, which hinders the practical use of MIBs. Third, large pore volumes of 3D graphene materials require additional volumes of electrolyte to infiltrate, thereby decreasing the energy densities of MIBs. Fourth, low densities of 3D graphene materials lead to low packing density and mass loading, which cannot meet the requirements for industry manufacturing. In addition, irrationally designed composite electrodes often cause low volumetric energy densities of MIBs. Last, the large voltage hysteresis of composite electrodes results in

the low energy efficiency of MIBs.

Aiming to develop advanced MIBs, future research directions should focus on the preparation of 3D graphene materials and rational designs of 3D graphene-based composite electrodes. As for preparation, feasible techniques to realize large-scale production of 3D graphene materials with high qualities and controllable structures are still required. As for constructing the 3D graphene-based composite electrodes, reducing the amount of 3D graphene materials is advisable to develop MIBs with high energy densities. In addition, in order to solve the issue of volume expansion during metal-ion insertion, voids should be specifically reserved and designed to accommodate the volume expansion of metal-host materials. Furthermore, a better understanding of metal-ion storage mechanisms in MIBs is still required to give more guidance for battery designs.

In conclusion, despite the current remaining issues, it is still very promising and inspiring to accelerate the industrialization process with tremendous efforts and change the landscape in energy storage technologies in the near future.

Conflicts of interest:

There are no conflicts of interest to declare.

Acknowledgements:

This work was fully supported by a grant from the Research Grants Council of the Hong Kong Special Administrative Region, China (Project No. 25211817).

References

1 A. K. Geim, *Science.*, 2009, **324**, 1530–1534.

2 X. Cao, Z. Yin and H. Zhang, , DOI:10.1039/c4ee00050a.

3 V. Chabot, D. Higgins, A. Yu, X. Xiao, Z. Chen and J. Zhang, *Energy Environ. Sci.*, 2014, **7**, 1564.

4 X. Huang, Z. Yin, S. Wu, X. Qi, Q. He, Q. Zhang, Q. Yan, F. Boey and H. Zhang, *Small*, 2011, **7**, 1876–1902.

5 X. Huang, X. Qi, F. Boey and H. Zhang, *Chem. Soc. Rev.*, 2012, **41**, 666–686.

6 J. Luo, H. D. Jang, T. Sun, L. Xiao, Z. He, A. P. Katsoulidis, M. G. Kanatzidis, J. M. Gibson and J. Huang, *ACS Nano*, 2011, **5**, 8943–8949.

7 Z. Dong, C. Jiang, H. Cheng, Y. Zhao, G. Shi, L. Jiang and L. Qu, *Adv. Mater.*, 2012, **24**, 1856–1861.

8 R. Wang, Y. Hao, Z. Wang, H. Gong and J. T. L. Thong, *Nano Lett.*, 2010, **10**, 4844–4850.

9 L. H. Viculis, J. J. Mack and R. B. Kaner, *Science.*, 2003, **299**, 1361.

10 Z. Chen, W. Ren, L. Gao, B. Liu, S. Pei and H. M. Cheng, *Nat. Mater.*, 2011, **10**, 424–428.

11 Y. Wu, P. Qiao, T. Chong and Z. Shen, *Adv. Mater.*, 2002, **14**, 64–67.

12 Y. Li, K. Yan, H.-W. Lee, Z. Lu, N. Liu and Y. Cui, *Nat. Energy*, 2016, **1**, 16017.

13 H. Wang, K. Sun, F. Tao, D. J. Stacchiola and Y. H. Hu, *Angew. Chemie. Int. Ed.*, 2013, **52**, 9210–9214.

14 D. Sun, J. Yang and X. Yan, *ChemElectroChem*, 2015, **2**, 348–353.

15 J. Luo, H. D. Jang and J. Huang, *ACS Nano*, 2013, **7**, 1464.

16 B. Wang, Q. Liu, J. Han, X. Zhang, J. Wang, Z. Li, H. Yan and L. Liu, *J.*

Mater. Chem. A, 2014, **2**, 1137–1143.

17 Z. Y. Yang, L. J. Jin, G. Q. Lu, Q. Q. Xiao, Y. X. Zhang, L. Jing, X. X. Zhang, Y. M. Yan and K. N. Sun, *Adv. Funct. Mater.*, 2014, **24**, 3917–3925.

18 Y. Li, K. Sheng, W. Yuan and G. Shi, *Chem. Commun.*, 2013, **49**, 291–293.

19 F. Han, O. Qian, B. Chen, H. Tang and M. Wang, *J. Alloys Compd.*, 2018, **730**, 386–391.

20 J. Sha, Y. Li, R. Villegas Salvatierra, T. Wang, P. Dong, Y. Ji, S. K. Lee, C. Zhang, J. Zhang, R. H. Smith, P. M. Ajayan, J. Lou, N. Zhao and J. M. Tour, *ACS Nano*, 2017, **11**, 6860–6867.

21 M. Yu, W. Qiu, F. Wang, T. Zhai, P. Fang, X. Lu and Y. Tong, *J. Mater. Chem. A*, 2015, **3**, 15792–15823.

22 X. Wu, D. Yang, C. Wang, Y. Jiang, T. Wei and Z. Fan, *Carbon.*, 2015, **92**, 26–30.

23 X. Jia, G. Zhang, T. Wang, X. Zhu, F. Yang, Y. Li, Y. Lu and F. Wei, *J. Mater. Chem. A*, 2015, **3**, 15738–15744.

24 D. Zhou, Y. Liu, W. L. Song, X. Li, L. Z. Fan and Y. Deng, *Chem. Eng. J.*, 2017, **316**, 645–654.

25 J. K. Lee, K. B. Smith, C. M. Hayner and H. H. Kung, *Chem. Commun.*, 2010, **46**, 2025.

26 X. H. Xia, D. L. Chao, Y. Q. Zhang, Z. X. Shen and H. J. Fan, *Nano Today*, 2014, **9**, 785–807.

27 H. Kim, J. Hong, G. Yoon, H. Kim, K. Park, M. Park, W. Yoon and K. Kang, *Energy Environ. Sci.*, 2015, **8**, 2963–2969.

28 C. Uthaisar, V. Barone and J. E. Peralta, *J. Appl. Phys.*, , DOI:10.1063/1.3265431.

29 S. Gong and Q. Wang, *J. Phys. Chem. C*, 2017, **121**, 24418–24424.

30 S. Li, J. Qiu, C. Lai, M. Ling, H. Zhao and S. Zhang, *Nano Energy*, 2015, **12**, 224–230.

31 X. Fan, X. Chen and L. Dai, *Curr. Opin. Colloid Interface Sci.*, 2015, **20**, 429–438.

32 R. Raccichini, A. Varzi, S. Passerini and B. Scrosati, *Nat. Mater.*, 2015, **14**, 271–279.

33 Y. Xu, G. Shi and X. Duan, *Acc. Chem. Res.*, 2015, **48**, 1666–1675.

34 J. E. Kim, J. H. Oh, M. Kotal, N. Koratkar and I. K. Oh, *Nano Today*, 2017, **14**, 100–123.

35 J.-J. Shao, W. Lv and Q.-H. Yang, *Adv. Mater.*, 2014, **26**, 5586–5612.

36 M. Chen, R. C. Haddon, R. Yan and E. Bekyarova, *Mater. Horizons*, 2017, **4**, 1054–1063.

37 X. Yao and Y. Zhao, *Chem*, 2017, **2**, 171–200.

38 M. Nazarian Samani, H. K. Kim, S. H. Park, H. C. Youn, D. Mhamane, S. W. Lee, M. S. Kim, J. H. Jeong, S. Haghighat Shishavan, K. C. Roh, S. F. Kashani Bozorg and K. B. Kim, *RSC Adv.*, 2016, **6**, 50941–50967.

39 Z. Yang, S. Chabi, Y. Xia and Y. Zhu, *Prog. Nat. Sci. Mater. Int.*, 2015, **25**, 554–562.

40 X. Cao, Z. Yin and H. Zhang, *Energy Environ. Sci.*, 2014, **7**, 1850–1865.

41 K.-Q. Lu, X. Xin, N. Zhang, Z.-R. Tang and Y.-J. Xu, *J. Mater. Chem. A*, 2018, **6**, 4590–4604.

42 B. Qiu, M. Xing and J. Zhang, *Chem. Soc. Rev.*, 2018, **47**, 2165–2216.

43 B. Luo and L. Zhi, *Energy Environ. Sci.*, 2015, **8**, 456–477.

44 J. Y. Liu, X. X. Li, J. R. Huang, J. J. Li, P. Zhou, J. H. Liu and X. J. Huang, *J.*

Mater. Chem. A, 2017, **5**, 5977–5994.

45 J. Zhu, J., Duan, R., Zhang, S., Jiang, N., Zhang, Y. and Zhu, *Springer Plus*, 2014, **3**, 1–8.

46 J. Zai and X. Qian, *RSC Adv.*, 2015, **5**, 8814–8834.

47 J. Xu, M. Wang, N. P. Wickramaratne, M. Jaroniec, S. Dou and L. Dai, *Adv. Mater.*, 2015, **27**, 2042–2048.

48 X. Liu, D. Chao, D. Su, S. Liu, L. Chen, C. Chi, J. Lin, Z. X. Shen, J. Zhao, L. Mai and Y. Li, *Nano Energy*, 2017, **37**, 108–117.

49 J. Li, Y. Zhang, T. Gao, J. Han, X. Wang, B. Hultman, P. Xu, Z. Zhang, G. Wu and B. Song, *J. Power Sources*, 2018, **378**, 105–111.

50 S. Wang, Z. Yu, J. Tu, J. Wang, D. Tian, Y. Liu and S. Jiao, *Adv. Energy Mater.*, 2016, **6**, 2–11.

51 Y. Hu, B. Luo, D. Ye, X. Zhu, M. Lyu and L. Wang, *Adv. Mater.*, 2017, **1606132**, 1606132–n/a.

52 X. Yu, B. Wang, D. Gong, Z. Xu and B. Lu, *Adv. Mater.*, , DOI:10.1002/adma.201604118.

53 G. Y. Yang, L. Chen, P. Jiang, Z. Y. Guo, W. Wang and Z. P. Liu, *RSC Adv.*, 2016, **6**, 47655–47660.

54 X. Huang, Y. Liu, H. Zhang, J. Zhang, O. Noonan and C. Yu, *J. Mater. Chem. A*, 2017, **5**, 19416–19421.

55 M. M. Islam, C. M. Subramaniyam, T. Akhter, S. N. Faisal, A. I. Minett, H. K. Liu, K. Konstantinov and S. X. Dou, *J. Mater. Chem. A*, 2017, **5**, 5290–5302.

56 X. Ma, G. Ning, Y. Sun, Y. Pu and J. Gao, *Carbon.*, 2014, **79**, 310–320.

57 Z. Sui, C. Wang, Q. Yang, K. Shu, Y. Liu, B. Han and G. G. Wallace, *J. Mater. Chem. A*, 2015, **3**, 18229–18237.

58 J. Zhang, B. Guo, Y. Yang, W. Shen, Y. Wang, X. Zhou, H. Wu and S. Guo, *Carbon.*, 2015, **84**, 469–478.

59 S. M. Yoon, W. M. Choi, H. Baik, H. J. Shin, I. Song, M. S. Kwon, J. J. Bae, H. Kim, Y. H. Lee and J. Y. Choi, *ACS Nano*, 2012, **6**, 6803–6811.

60 Z. Jiang, Z. J. Jiang, X. Tian and L. Luo, *Electrochim. Acta*, 2014, **146**, 455–463.

61 Z. J. Jiang and Z. Jiang, *ACS Appl. Mater. Interfaces*, 2014, **6**, 19082–19091.

62 Q. Chen, C. Zhang, F. Xue, Y. Zhou, W. Li, Y. Wang, W. Tu, Z. Zou, X. Wang and M. Xiao, *Sci. Rep.*, 2013, **3**, 1–7.

63 W. Fan, Y. Y. Xia, W. W. Tjiu, P. K. Pallathadka, C. He and T. Liu, *J. Power Sources*, 2013, **243**, 973–981.

64 J. Le Shi, H. J. Peng, L. Zhu, W. Zhu and Q. Zhang, *Carbon.*, 2015, **92**, 96–105.

65 P. Guo, H. Song and X. Chen, *J. Mater. Chem.*, 2010, **20**, 4867.

66 Y. Ding, H. Cheng, C. Zhou, Y. Fan, J. Zhu, H. Shao and L. Qu, *Nanotechnology*, , DOI:10.1088/0957-4484/23/25/255605.

67 L. Xiao, J. Damien, J. Luo, H. D. Jang, J. Huang and Z. He, *J. Power Sources*, 2012, **208**, 187–192.

68 Z. Tang, X. Li, Z. Han, L. Yao, S. Shen and J. Yang, *RSC Adv.*, 2016, **6**, 87796–87801.

69 R. Wang, W. Guo, X. Li, Z. Liu, H. Liu and S. Ding, *J. Mater. Sci.*, 2017, **52**, 13930–13939.

70 X. Dou, A. R. Koltonow, X. He, H. D. Jang, Q. Wang, Y.-W. Chung and J. Huang, *Proc. Natl. Acad. Sci.*, 2016, **113**, 1528–1533.

71 Z. Xu, H. Sun, X. Zhao and C. Gao, *Adv. Mater.*, 2013, **25**, 188–193.

72 Z. Xu, Y. Zhang, P. Li and C. Gao, *ACS Nano*, 2012, **6**, 7103–7113.

73 H. Cheng, C. Hu, Y. Zhao and L. Qu, *NPG Asia Mater.*, 2014, **6**, 113.

74 M. Zhou, T. Lin, F. Huang, Y. Zhong, Z. Wang, Y. Tang, H. Bi, D. Wan and J. Lin, *Adv. Funct. Mater.*, 2013, **23**, 2263–2269.

75 Q. Li, P. Xu, W. Gao, S. Ma, G. Zhang, R. Cao, J. Cho, H. L. Wang and G. Wu, *Adv. Mater.*, 2014, **26**, 1378–1386.

76 Q. Li, H. Pan, D. Higgins, R. Cao, G. Zhang, H. Lv, K. Wu, J. Cho and G. Wu, *Small*, 2015, **11**, 1443–1452.

77 F. Zeng, Y. Kuang, Y. Wang, Z. Huang, C. Fu and H. Zhou, *Adv. Mater.*, 2011, **23**, 4929–4932.

78 F. Zeng, Y. Kuang, G. Liu, R. Liu, Z. Huang, C. Fu and H. Zhou, *Nanoscale*, 2012, **4**, 3997.

79 Y. Shi, W. Gao, H. Lu, Y. Huang, L. Zuo, W. Fan and T. Liu, *ACS Sustain. Chem. Eng.*, 2017, **5**, 6994–7002.

80 M. Hiramatsu, K. Shiji, H. Amano and M. Hori, *Appl. Phys. Lett.*, 2004, **84**, 4708–4710.

81 K. Yu, Z. Bo, G. Lu, S. Mao, S. Cui, Y. Zhu, X. Chen, R. S. Ruoff and J. Chen, *Nanoscale Res. Lett.*, 2011, **6**, 202.

82 K. Davami, Y. Jiang, J. Cortes, C. Lin, M. Shaygan, K. T. Turner and I. Bargatin, *Nanotechnology*, , DOI:10.1088/0957-4484/27/15/155701.

83 C. Lin, K. Davami, Y. Jiang, J. Cortes, M. Munther, M. Shaygan, H. Ghassemi, J. T. Robinson, K. T. Turner and I. Bargatin, *Nanotechnology*, , DOI:10.1088/1361-6528/aa75ac.

84 A. Wu, X. Li, J. Yang, C. Du, W. Shen and J. Yan, *Nanomaterials*, 2017, **7**, 318.

85 K. Yu, G. Lu, Z. Bo, S. Mao and J. Chen, *J. Phys. Chem. Lett.*, 2011, **2**, 1556–1562.

86 N. G. Shang, P. Papakonstantinou, M. McMullan, M. Chu, A. Stamboulis, A. Potenza, S. S. Dhesi and H. Marchetto, *Adv. Funct. Mater.*, 2008, **18**, 3506–3514.

87 R. Garg, S. K. Rastogi, M. Lamparski, S. C. De La Barrera, G. T. Pace, N. T. Nuhfer, B. M. Hunt, V. Meunier and T. Cohen-Karni, *ACS Nano*, 2017, **11**, 6301–6311.

88 M. A. Azam, N. N. Zulkapli, N. Dorah, R. N. A. R. Seman, M. H. Ani, M. S. Sirat, E. Ismail, F. B. Fauzi, M. A. Mohamed and B. Y. Majlis, *ECS J. Solid State Sci. Technol.*, 2017, **6**, 3035–3048.

89 M. Li, D. Liu, D. Wei, X. Song, D. Wei and A. T. S. Wee, *Adv. Sci.*, 2016, **3**, 1–23.

90 L. Zhao, Y. Qiu, J. Yu, X. Deng, C. Dai and X. Bai, *Nanoscale*, 2013, **5**, 4902.

91 J. Zeng, X. Ji, Y. Ma, Z. Zhang, S. Wang, Z. Ren, C. Zhi and J. Yu, *Adv. Mater.*, 2018, **30**, 1705380.

92 R. Zhang, Y. Cao, P. Li, X. Zang, P. Sun, K. Wang, M. Zhong, J. Wei, D. Wu, F. Kang and H. Zhu, *Nano Res.*, 2014, **7**, 1477–1487.

93 W. Fang, N. Zhang, L. Fan and K. Sun, *J. Power Sources*, 2016, **333**, 30–36.

94 L. Hu, X. Peng, Y. Li, L. Wang, K. Huo, L. Y. S. Lee, K. Y. Wong and P. K. Chu, *Nano Energy*, 2017, **34**, 515–523.

95 C. L. Yuxi Xu, Kaixuan Sheng and G. Shi, *ACS Nano*, 2010, **4**, 4324–4330.

96 H. Hu, Z. Zhao, W. Wan, Y. Gogotsi and J. Qiu, *Adv. Mater.*, 2013, **25**, 2219–2223.

97 J. Chang, X. Huang, G. Zhou, S. Cui, P. B. Hallac, J. Jiang, P. T. Hurley and J.

Chen, *Adv. Mater.*, 2014, **26**, 758–764.

98 L. Jing, H. L. Tan, R. Amal, Y. H. Ng and K.-N. Sun, *J. Mater. Chem. A*, 2015, **3**, 15675–15682.

99 H. Zhu, X. Wu, L. Zan and Y. Zhang, *ACS Appl. Mater. Interfaces*, 2014, **6**, 11724–33.

100 S. Mao, K. Yu, J. Chang, D. A. Steeber, L. E. Ocola and J. Chen, *Sci. Rep.*, 2013, **3**, 33–36.

101 Z. Yan, W. Yao, L. Hu, D. Liu, C. Wang and C. Lee, *Nanoscale*, 2015, **7**, 5563–5577.

102 Z. Sun, W. Fan and T. Liu, *Electrochim. Acta*, 2017, **250**, 91–98.

103 L. Zhong, C. Tang, B. Wang, H.-F. Wang, S. Gao, Y. Wang and Q. Zhang, *New Carbon Mater.*, 2017, **32**, 509–516.

104 X. Dong, H. Xu, X. Wang, Y. Huang, M. B. Chan-park and H. Zhang, *ACS Nano*, 2012, 3206–3213.

105 G. Zhou, J. Sun, Y. Jin, W. Chen, C. Zu, R. Zhang, Y. Qiu, J. Zhao, D. Zhuo, Y. Liu, X. Tao, W. Liu, K. Yan, H. R. Lee and Y. Cui, *Adv. Mater.*, , DOI:10.1002/adma.201603366.

106 J. Han, D. Kong, W. Lv, D. Tang, D. Han, C. C. Zhang, D. Liu, Z. Xiao, X. Zhang, J. Xiao, X. He, F. Hsia, C. C. Zhang, Y. Tao, D. Golberg, F. Kang, L. Zhi and Q. Yang, *Nat. Commun.*, 2018, **9**, 402.

107 L. Chang, W. Wei, K. Sun and Y. H. Hu, *J. Mater. Chem. A*, 2015, **3**, 10183–10187.

108 N. Li, X. Huang, H. Zhang, Z. Shi and C. Wang, *J. Mater. Chem. A*, 2017, 16803–16811.

109 X. Wang, Y. Zhang, C. Zhi, X. Wang, D. Tang, Y. Xu, Q. Weng, X. Jiang, M.

Mitome, D. Golberg and Y. Bando, *Nat. Commun.*, 2013, **4**, 1–8.

110 Y. Zhu, G. Chen, Y. Zhong, W. Zhou and Z. Shao, *Adv. Sci.*, 2018, **5**, 1700603.

111 Y. Zhao, Y. Zhou, B. Xiong, J. Wang, X. Chen, R. O'Hayre and Z. Shao, *J. Solid State Electrochem.*, 2013, **17**, 1089–1098.

112 B. Zhao, Y. Zheng, F. Ye, X. Deng, X. Xu, M. Liu and Z. Shao, *ACS Appl. Mater. Interfaces*, 2015, **7**, 14446–14455.

113 B. Xiong, Y. Zhou, Y. Zhao, J. Wang, X. Chen, R. O'Hayre and Z. Shao, *Carbon N. Y.*, 2013, **52**, 181–192.

114 J. Wang, Y. Zhou, B. Xiong, Y. Zhao, X. Huang and Z. Shao, *Electrochim. Acta*, 2013, **88**, 847–857.

115 B. Xiong, Y. Zhou, Y. Zhao, J. Wang, X. Chen, R. O'Hayre and Z. Shao, *Carbon N. Y.*, 2013, **52**, 181–192.

116 G. Wu, Y. Zhou and Z. Shao, *Appl. Surf. Sci.*, 2013, **283**, 999–1005.

117 X. Deng, B. T. Zhao, L. Zhu and Z. P. Shao, *Carbon N. Y.*, 2015, **93**, 48–58.

118 P. Tan, M. Liu, Z. Shao and M. Ni, *Adv. Energy Mater.*, 2017, **7**, 1–23.

119 J. Yu, G. Chen, J. Sunarso, Y. Zhu, R. Ran, Z. Zhu, W. Zhou and Z. Shao, *Adv. Sci.*, 2016, **3**, 1–8.

120 P. Tan, W. Kong, Z. Shao, M. Liu and M. Ni, *Prog. Energy Combust. Sci.*, 2017, **62**, 155–189.

121 B. Zhao, S. Jiang, C. Su, R. Cai, R. Ran, M. O. Tadé and Z. Shao, *J. Mater. Chem. A*, 2013, **1**, 12310–12320.

122 Y. Liu, Z. Wang, Y. Zhong, M. Tade, W. Zhou and Z. Shao, *Adv. Funct. Mater.*, 2017, **27**, 1–10.

123 W. Wang, X. Xu, W. Zhou and Z. Shao, *Adv. Sci.*, 2017, **4**, 1600371.

124 X. Duan, C. Su, L. Zhou, H. Sun, A. Suvorova, T. Odedairo, Z. Zhu, Z. Shao

and S. Wang, *Appl. Catal. B Environ.*, 2016, **194**, 7–15.

125 P. R. Somani, S. P. Somani and M. Umeno, *Chem. Phys. Lett.*, 2006, **430**, 56–59.

126 Z. Wu, W. Wang, Y. Wang, C. Chen, K. Li, G. Zhao, C. Sun, W. Chen, L. Ni and G. Diao, *Electrochim. Acta*, 2017, **224**, 527–533.

127 J. S. Lee, S. I. Kim, J. C. Yoon and J. H. Jang, *ACS Nano*, 2013, **7**, 6047–6055.

128 K. Qin, E. Liu, J. Li, J. Kang, C. Shi, C. He, F. He and N. Zhao, *Adv. Energy Mater.*, 2016, **6**, 1–10.

129 C. Tang, H. Sen Wang, H. F. Wang, Q. Zhang, G. L. Tian, J. Q. Nie and F. Wei, *Adv. Mater.*, 2015, **27**, 4516–4522.

130 L. Liu, Y. Yin, J. Li, S. Wang, Y. Guo and L. Wan, *Adv. Mater.*, 2018, **30**, 1706216.

131 Z. S. Wu, Y. Sun, Y. Z. Tan, S. Yang, X. Feng and K. M??llen, *J. Am. Chem. Soc.*, 2012, **134**, 19532–19535.

132 F. Liu and T. K. Seo, *Adv. Funct. Mater.*, 2010, **20**, 1930–1936.

133 F. Liu, S. Chung, G. Oh and T. S. Seo, 2012, 1–2.

134 H. D. Jang, S. K. Kim, H. Chang, J. H. Choi, B. G. Cho, E. H. Jo, J. W. Choi and J. Huang, *Carbon N. Y.*, 2015, **93**, 869–877.

135 Q. Li, Z. Li, Z. Zhang, C. Li, J. Ma, C. Wang, X. Ge, S. Dong and L. Yin, *Adv. Energy Mater.*, 2016, **6**, 1–10.

136 M. Lao, Y. Zhang, W. Luo, Q. Yan, W. Sun and S. X. Dou, *Adv. Mater.*, 2017, **29**, 1–23.

137 J. Li, S. Zhao, G. Zhang, Y. Gao, L. Deng, R. Sun and C.-P. Wong, *J. Mater. Chem. A*, 2015, **3**, 15482–15488.

138 S. Li, M. Wang and Y. Lian, *Sci. China Chem.*, 2016, **59**, 405–411.

139 G. Luo, H. Huang, C. Lei, Z. Cheng, X. Wu, S. Tang and Y. Du, *Appl. Surf. Sci.*, 2016, **366**, 46–52.

140 Y. Zhao, Y. Zhou, R. O. Hayre and Z. Shao, *J. Phys. Chem. Solids*, 2013, **74**, 1608–1614.

141 A. R. Kamali, *J. Ind. Eng. Chem.*, 2017, **52**, 18–27.

142 S. Wan, H. Bi, X. Xie, S. Su, K. Du, H. Jia, T. Xu, L. He, K. Yin and L. Sun, *Sci. Rep.*, 2016, **6**, 1–7.

143 M. F. El-Kady, V. Strong, S. Dubin and R. B. Kaner, *Science (80-.).*, 2012, **335**, 1326–1330.

144 V. Strong, S. Dubin, M. F. El-Kady, A. Lech, Y. Wang, B. H. Weiller and R. B. Kaner, *ACS Nano*, 2012, **6**, 1395–1403.

145 C. Zhu, P. Kopold, P. A. Van Aken, J. Maier and Y. Yu, *Adv. Mater.*, 2016, **28**, 2409–2416.

146 H. Chen, H. Xu, S. Wang, T. Huang, J. Xi, S. Cai, F. Guo, Z. Xu, W. Gao and C. Gao, *Sci. Adv.*, 2017, **3**, 7233.

147 Y. Liu, L. Z. Fan and L. Jiao, *J. Power Sources*, 2017, **340**, 104–110.

148 J. R. Dahn, T. Zheng, Y. Liu and J. S. Xue, *Science.*, 1995, **270**, 590–593.

149 E. Pollak, B. Geng, K. J. Jeon, I. T. Lucas, T. J. Richardson, F. Wang and R. Kostecki, *Nano Lett.*, 2010, **10**, 3386–3388.

150 E. Lee and K. A. Persson, *Nano Lett.*, 2012, **12**, 4624–4628.

151 L. L. Tian, Q. C. Zhuang, J. Li, Y. L. Shi, J. P. Chen, F. Lu and S. G. Sun, *Chinese Sci. Bull.*, 2011, **56**, 3204–3212.

152 L. Jiao, T. Wu, H. Li, F. Li and L. Niu, *Chem. Commun.*, 2015, **51**, 15979–15981.

153 X. Deng, K. Xie, L. Li, W. Zhou, J. Sunarso and Z. Shao, *Carbon N. Y.*, 2016,

107, 67–73.

154 B. Jache and P. Adelhelm, *Angew. Chemie - Int. Ed.*, 2014, **53**, 10169–10173.

155 H. Kim, J. Hong, Y. U. Park, J. Kim, I. Hwang and K. Kang, *Adv. Funct. Mater.*, 2015, **25**, 534–541.

156 Y. Cao, L. Xiao, M. L. Sushko, W. Wang, B. Schwenzer, J. Xiao, Z. Nie, L. V. Saraf, Z. Yang and J. Liu, *Nano Lett.*, 2012, **12**, 3783–3787.

157 J. Ding, H. Wang, Z. Li, A. Kohandehghan, K. Cui, Z. Xu, B. Zahiri, X. Tan, E. M. Lotfabad, B. C. Olsen and D. Mitlin, *ACS Nano*, 2013, **7**, 11004–11015.

158 W. Luo, J. Wan, B. Ozdemir, W. Bao, Y. Chen, J. Dai, H. Lin, Y. Xu, F. Gu, V. Barone and L. Hu, *Nano Lett.*, 2015, **15**, 7671–7677.

159 Z. A. Zafar, S. Imtiaz, R. Razaq, S. Ji, T. Huang, Z. Zhang, Y. Huang and J. A. Anderson, *J. Mater. Chem. A*, 2017, **5**, 5646–5660.

160 S. K. Das, S. Mahapatra and H. Lahan, *J. Mater. Chem. A*, 2017, **5**, 6347–6367.

161 M. C. Lin, M. Gong, B. Lu, Y. Wu, D. Y. Wang, M. Guan, M. Angell, C. Chen, J. Yang, B. J. Hwang and H. Dai, *Nature*, 2015, **520**, 325–328.

162 H. Chen, C. Chen, Y. Liu, X. Zhao, N. Ananth, B. Zheng, L. Peng, T. Huang, W. Gao and C. Gao, *Adv. Energy Mater.*, 2017, **7**, 1–9.

163 Y. Liu, J. S. Xue, T. Zheng and J. R. Dahn, *Carbon N. Y.*, 2017, **0728**, 3123129.

164 F. J. Sonia, M. K. Jangid, B. Ananthoju, M. Aslam, P. Johari and A. Mukhopadhyay, *J. Mater. Chem. A*, 2017, **5**, 8662–8679.

165 Y. Liu, V. I. Artyukhov, M. Liu, A. R. Harutyunyan and B. I. Yakobson, *J. Phys. Chem. Lett.*, 2013, **4**, 1737–1742.

166 X. Wang, Q. Weng, X. Liu, X. Wang, D. M. Tang, W. Tian, C. Zhang, W. Yi, D. Liu, Y. Bando and D. Golberg, *Nano Lett.*, 2014, **14**, 1164–1171.

167 Y. A. Kim, T. Hayashi, J. H. Kim and M. Endo, *J. Energy Chem.*, 2013, **22**, 183–194.

168 C. Uthaisar and V. Barone, *Nano Lett.*, 2010, **10**, 2838–2842.

169 P. Bai, Y. He, X. Zou, X. Zhao, P. Xiong and Y. Xu, *Adv. Energy Mater.*, 2018, **8**, 1703217.

170 Y. Li, Y. Hu, X. Qi, X. Rong and H. Li, *Energy Storage Mater.*, 2016, **5**, 191–197.

171 Y. S. Yun, K. Y. Park, B. Lee, S. Y. Cho, Y. U. Park, S. J. Hong, B. H. Kim, H. Gwon, H. Kim, S. Lee, Y. W. Park, H. J. Jin and K. Kang, *Adv. Mater.*, 2015, **27**, 6914–6921.

172 C. Bommier, T. W. Surta, M. Dolgos and X. Ji, *Nano Lett.*, 2015, **15**, 5888–5892.

173 K. Share, A. P. Cohn, R. Carter, B. Rogers and C. L. Pint, *ACS Nano*, 2016, **10**, 9738–9744.

174 G. Ma, K. Huang, J.-S. Ma, Z. Ju, Z. Xing and Q. Zhuang, *J. Mater. Chem. A*, 2017, **5**, 7854–7861.

175 Z. Ju, S. Zhang, Z. Xing, Q. Zhuang, Y. Qiang and Y. Qian, *ACS Appl. Mater. Interfaces*, 2016, **8**, 20682–20690.

176 Y. Xiao, S. H. Lee and Y. K. Sun, *Adv. Energy Mater.*, 2017, **7**, 1601329.

177 J. Zhu, T. Wang, F. Fan, L. Mei and B. Lu, *ACS Nano*, 2016, **10**, 8243–8251.

178 P. Chang, X. Liu, Q. Zhao, Y. Huang, Y. Huang and X. Hu, *ACS Appl. Mater. Interfaces*, 2017, **9**, 31879–31886.

179 J. Luo, X. Zhao, J. Wu, H. D. Jang, H. H. Kung and J. Huang, *J. Phys. Chem. Lett.*, 2012, **3**, 1824–1829.

180 N. Kim, C. Oh, J. Kim, J. S. Kim, E. D. Jeong, J. S. Bae, T. E. Hong and J. K.

Lee, *J. Electrochem. Soc.*, 2017, **164**, A6075–A6083.

181 B. Lee, T. Liu, S. K. Kim, H. Chang, K. Eom, L. Xie, S. Chen, H. D. Jang and S. W. Lee, *Carbon.*, 2017, **119**, 438–445.

182 D. Li, K. H. Seng, D. Shi, Z. Chen, H. K. Liu and Z. Guo, *J. Mater. Chem. A*, 2013, **1**, 14115.

183 H. Kim, Y. Son, C. Park, J. Cho and H. C. Choi, *Angew. Chemie. Int. Ed.*, 2013, **52**, 5997–6001.

184 Y. Xu, X. Zhu, X. Zhou, X. Liu, Y. Liu, Z. Dai and J. Bao, *J. Phys. Chem. C*, 2014, **118**, 28502–28508.

185 S. Fang, L. Shen, H. Zheng and X. Zhang, *J. Mater. Chem. A*, 2015, **3**, 1498–1503.

186 J. Ren, Q. Wu, H. Tang, G. Hong, W. Zhang and S. Lee, *J. Mater. Chem. A*, 2013, **1**, 1821–1826.

187 C. Wang, J. Ju, Y. Yang, Y. Tang, J. Lin, Z. Shi, R. P. S. Han and F. Huang, *J. Mater. Chem. A*, 2013, **1**, 8897.

188 R. Mo, D. Rooney, K. Sun and H. Y. Yang, *Nat. Commun.*, 2017, **8**, 1–9.

189 G. Ren, M. N. F. Hoque, J. Liu, J. Warzywoda and Z. Fan, *Nano Energy*, 2016, **21**, 162–171.

190 F. Ye, B. Zhao, R. Ran and Z. Shao, *Chem. - A Eur. J.*, 2014, **20**, 4055–4063.

191 Y. Huang, D. Wu, J. Wang, S. Han, L. Lv, F. Zhang and X. Feng, *Small*, 2014, **10**, 2226–2232.

192 S. Jiang, B. Zhao, R. Ran, R. Cai, M. O. Tadé and Z. Shao, *RSC Adv.*, 2014, **4**, 9367–9371.

193 M. Zhang, E. Liu, T. Cao, H. Wang, C. Shi, J. Li, C. He, F. He, L. Ma and N. Zhao, *J. Mater. Chem. A*, 2017, **5**, 7035–7042.

194 J. Wang, J. Liu, D. Chao, J. Yan, J. Lin and Z. X. Shen, *Adv. Mater.*, 2014, **26**, 7162–7169.

195 Y. Chao, R. Jalili, Y. Ge, C. Wang, T. Zheng, K. Shu and G. G. Wallace, *Adv. Funct. Mater.*, 2017, **27**, 1–10.

196 K. Chang, Z. Wang, G. Huang, H. Li, W. Chen and J. Y. Lee, *J. Power Sources*, 2012, **201**, 259–266.

197 H. Tang, X. Qi, Z. Zhang, G. Ai, Y. Liu, Z. Huang and J. Zhong, *Ceram. Int.*, 2015, **42**, 6572–6580.

198 B. Zhao, Z. Wang, F. Chen, Y. Yang, Y. Gao, L. Chen, Z. Jiao, L. Cheng and Y. Jiang, *ACS Appl. Mater. Interfaces*, 2017, **9**, 1407–1415.

199 N. Li, Z. ping Chen, W. cai Ren, F. Li and H. ming Chen, *Proc. Natl. Acad. Sci.*, 2012, **109**, 17360–17365.

200 G. Wang, B. Wang, X. Wang, J. Park, S. Dou, H. Ahn and K. Kim, *J. Mater. Chem.*, 2009, **19**, 8378.

201 Q. Fang, Y. Shen and B. Chen, *Chem. Eng. J.*, 2015, **264**, 753–771.

202 T. Yuan, W. T. Li, W. Zhang, Y. S. He, C. Zhang, X. Z. Liao and Z. F. Ma, *Ind. Eng. Chem. Res.*, 2014, **53**, 10849–10857.

203 S. M. Bak, K. W. Nam, C. W. Lee, K. H. Kim, H. C. Jung, X. Q. Yang and K. B. Kim, *J. Mater. Chem.*, 2011, **21**, 17309.

204 R. Jiang, C. Cui and H. Ma, *Phys. Chem. Chem. Phys.*, 2013, **15**, 6406.

205 D. Rangappa, K. D. Murukanahally, T. Tomai, A. Unemoto and I. Honma, *Nano Lett.*, 2012, **12**, 1146–1151.

206 K. Amin, Q. Meng, A. Ahmad, M. Cheng, M. Zhang, L. Mao, K. Lu and Z. Wei, *Adv. Mater.*, 2017, **1703868**, 1–8.

207 G. Yang, F. Bu, Y. Huang, Y. Zhang, I. Shakir and Y. Xu, *ChemSusChem*,

2017, 3419–3426.

208 H. Liu, G. Yang, X. Zhang, P. Gao, L. Wang, J. Fang, J. Pinto and X. Jiang, *J. Mater. Chem.*, 2012, **22**, 11039.

209 I. H. Son, J. H. Park, S. Park, K. Park, S. Han, J. Shin, S. G. Doo, Y. Hwang, H. Chang and J. W. Choi, *Nat. Commun.*, 2017, **8**, 1–10.

210 K. C. Jiang, S. Xin, J. S. Lee, J. Kim, X. L. Xiao and Y. G. Guo, *Phys. Chem. Chem. Phys.*, 2012, **14**, 2934.

211 Y. Huang, K. Li, J. Liu, X. Zhong, X. Duan, I. Shakir and Y. Xu, *J. Mater. Chem. A*, 2017, **5**, 2710–2716.

212 J. Patra, H. C. Chen, C. H. Yang, C. Te Hsieh, C. Y. Su and J. K. Chang, *Nano Energy*, 2016, **28**, 124–134.

213 D. Su, H. J. Ahn and G. Wang, *Chem. Commun.*, 2013, **49**, 3131.

214 H. Liu, M. Jia, Q. Zhu, B. Cao, R. Chen, Y. Wang, F. Wu and B. Xu, *ACS Appl. Mater. Interfaces*, 2016, **8**, 26878–26885.

215 S. H. Choi, Y. N. Ko, J. K. Lee and Y. C. Kang, *Adv. Funct. Mater.*, 2015, **25**, 1780–1788.

216 C. Wu, P. Kopold, P. A. van Aken, J. Maier and Y. Yu, *Adv. Mater.*, 2017, **29**, 1–7.

217 X. Wang, K. Chen, G. Wang, X. Liu and H. Wang, *ACS Nano*, 2017, **11**, 11602–11616.

218 X. Ge, Z. Li and L. Yin, *Nano Energy*, 2017, **32**, 117–124.

219 Z. Zhou, H. Xiao, F. Zhang, X. Zhang and Y. Tang, *Electrochim. Acta*, 2016, **211**, 430–436.

220 D. Zhou, X. Li, L. Z. Fan and Y. Deng, *Electrochim. Acta*, 2017, **230**, 212–221.

221 K. Xie, L. Li, X. Deng, W. Zhou and Z. Shao, *J. Alloys Compd.*, 2017, **726**, 394–402.

222 Y. Liu, Z. Cheng, H. Sun, H. Arandiyan, J. Li and M. Ahmad, *J. Power Sources*, 2015, **273**, 878–884.

223 S. M. B, S. AL, A. J. Bhattacharyya and C. N. R. Rao, *J. Mater. Chem. A*, 2016, **4**, 9466–9471.

224 N. Li, S. Liao, Y. Sun, H. W. Song and C. X. Wang, *J. Mater. Chem. A*, 2015, **3**, 5820–5828.

225 Y. Liu, H. Kang, L. Jiao, C. Chen, K. Cao, Y. Wang and H. Yuan, *Nanoscale*, 2015, **7**, 1325–1332.

226 X. Xiong, C. Yang, G. Wang, Y. Lin, X. Ou, J. H. Wang, B. Zhao, M. Liu, Z. Lin and K. Huang, *Energy Environ. Sci.*, 2017, 1757–1763.

227 J. Qian, Y. Xiong, Y. Cao, X. Ai and H. Yang, *Nano Lett.*, 2014, **14**, 1865–1869.

228 F. Pan, W. Zhang, J. Ma, N. Yao, L. Xu, Y. S. He, X. Yang and Z. F. Ma, *Electrochim. Acta*, 2016, **196**, 572–578.

229 C. Wu, P. Kopold, Y. L. Ding, P. A. Van Aken, J. Maier and Y. Yu, *ACS Nano*, 2015, **9**, 6610–6618.

230 Z. Liu, Y. Zhang, H. Zhao, N. Li and Y. Du, *Sci. China Mater.*, 2017, **60**, 167–177.

231 Y. Jiang, H. Zhang, H. Yang, Z. Qi and Y. Yu, *Nanoscale*, 2017, **9**, 6048–6055.

232 J. Fang, S. Wang, Z. Li, H. Chen, L. Xia, L. Ding and H. Wang, *J. Mater. Chem. A*, 2016, **4**, 1180–1185.

233 X. Rui, W. Sun, C. Wu, Y. Yu and Q. Yan, *Adv. Mater.*, 2015, **27**, 6670–6676.

234 H. Jin, M. Liu, E. Uchaker, J. Dong, Q. Zhang, S. Hou, J. Li and G. Cao, *CrystEngComm*, 2017, **19**, 4287–4293.

235 H. Jin, J. Dong, E. Uchaker, Q. Zhang, X. Zhou, S. Hou, J. Li and G. Cao, *J. Mater. Chem. A*, 2015, **3**, 17563–17568.

236 S. Zhang, C. Deng and Y. Meng, *J. Mater. Chem. A*, 2014, **2**, 20538–20544.

237 Y. Zhang, Y. Huang, G. Yang, F. Bu, K. Li, I. Shakir and Y. Xu, *ACS Appl. Mater. Interfaces*, 2017, **9**, 15549–15556.

238 V. Lakshmi, Y. Chen, A. A. Mikhaylov, A. G. Medvedev, I. Sultana, M. M. Rahman, O. Lev, P. V. Prikhodchenko and A. M. Glushenkov, *Chem. Commun.*, 2017, **53**, 8272–8275.

239 Y. Lu and J. Chen, *Sci. China Chem.*, 2017, **60**, 1533–1539.

240 H. Gao, T. Zhou, Y. Zheng, Q. Zhang, Y. Liu, J. Chen, H. Liu and Z. Guo, *Adv. Funct. Mater.*, 2017, **27**, 1–9.

241 K. Xie, K. Yuan, X. Li, W. Lu, C. Shen, C. Liang, R. Vajtai, P. Ajayan and B. Wei, *Small*, 2017, **13**, 1–8.

242 H. D. Yoo, I. Shterenberg, Y. Gofer, G. Gershinsky, N. Pour and D. Aurbach, *Energy Environ. Sci.*, 2013, **6**, 2265.

243 J. Muldoon, C. B. Bucur and T. Gregory, *Chem. Rev.*, 2014, **114**, 11683–11720.

244 Q. An, Y. Li, H. Deog Yoo, S. Chen, Q. Ru, L. Mai and Y. Yao, *Nano Energy*, 2015, **18**, 265–272.

245 S. H. Lee, R. A. DiLeo, A. C. Marschilok, K. J. Takeuchi and E. S. Takeuchi, *ECS Electrochem. Lett.*, 2014, **3**, A87–A90.

246 H. Zhang, K. Ye, K. Zhu, R. Cang, X. Wang, G. Wang and D. Cao, *ACS Sustain. Chem. Eng.*, 2017, **5**, 6727–6735.

247 E. M. Kamar and E. Sheha, *Mater. Sci. Pol.*, 2017, **35**, 528–533.

248 Y. Zhang, P. Chen, X. Gao, B. Wang, H. H. Liu, H. Wu, H. H. Liu and S. Dou, *Adv. Funct. Mater.*, 2016, **26**, 7754–7765.

249 X. Hu, G. Zeng, J. Chen, C. Lu and Z. Wen, *J. Mater. Chem. A*, 2017, **5**, 4535–4542.

250 B. Yan, X. Li, Z. Bai, Y. Zhao, L. Dong, X. Song, D. Li, C. Langford and X. Sun, *Nano Energy*, 2016, **24**, 32–44.

251 H. Liu and W. Yang, *Energy Environ. Sci.*, 2011, **4**, 4000.

252 K. Palanisamy, J. H. Um, M. Jeong and W. S. Yoon, *Sci. Rep.*, 2016, **6**, 1–12.

253 B. Wu, G. Li and F. Liu, *Int. J. Hydrogen Energy*, 2017, **42**, 21849–21854.

254 L. Pei, Q. Zhao, C. Chen, J. Liang and J. Chen, *ChemElectroChem*, 2015, **2**, 1652–1655.

255 G.-H. Lee, M. R. Jo, K. Zhang and Y.-M. Kang, *J. Mater. Chem. A*, 2017, **5**, 3683–3690.

256 B. Yan, X. Li, Z. Bai, L. Lin, G. Chen, X. Song, D. Xiong, D. Li and X. Sun, *J. Mater. Chem. A*, 2017, **5**, 4850–4860.

257 Y. Wang, H. Huang, Q. Xie, Y. Wang and B. Qu, *J. Alloys Compd.*, 2017, **705**, 314–319.

258 C. Chen, H. Xu, T. Zhou, Z. Guo, L. Chen, M. Yan, L. Mai, P. Hu, S. Cheng, Y. Huang and J. Xie, *Adv. Energy Mater.*, 2016, **6**, 2–9.

259 Y. Yin, F. Xiong, C. Pei, Y. Xu, Q. An, S. Tan, Z. Zhuang, J. Sheng, Q. Li and L. Mai, *Nano Energy*, 2017, **41**, 452–459.

260 S. Tao, X. Wang, P. Cui, Y. Wang, Y. A. Haleem, S. Wei, W. Huang, L. Song and W. Chu, *RSC Adv.*, 2016, **6**, 43591–43597.

261 H. J. Yen, H. Tsai, M. Zhou, E. F. Holby, S. Choudhury, A. Chen, L. Adamska,

S. Tretiak, T. Sanchez, S. Iyer, H. Zhang, L. Zhu, H. Lin, L. Dai, G. Wu and H. L. Wang, *Adv. Mater.*, 2016, **28**, 10250–10256.

262 Z. Bo, S. Mao, Z. Jun Han, K. Cen, J. Chen and K. (Ken) Ostrikov, *Chem. Soc. Rev.*, 2015, **44**, 2108–2121.

Figures:

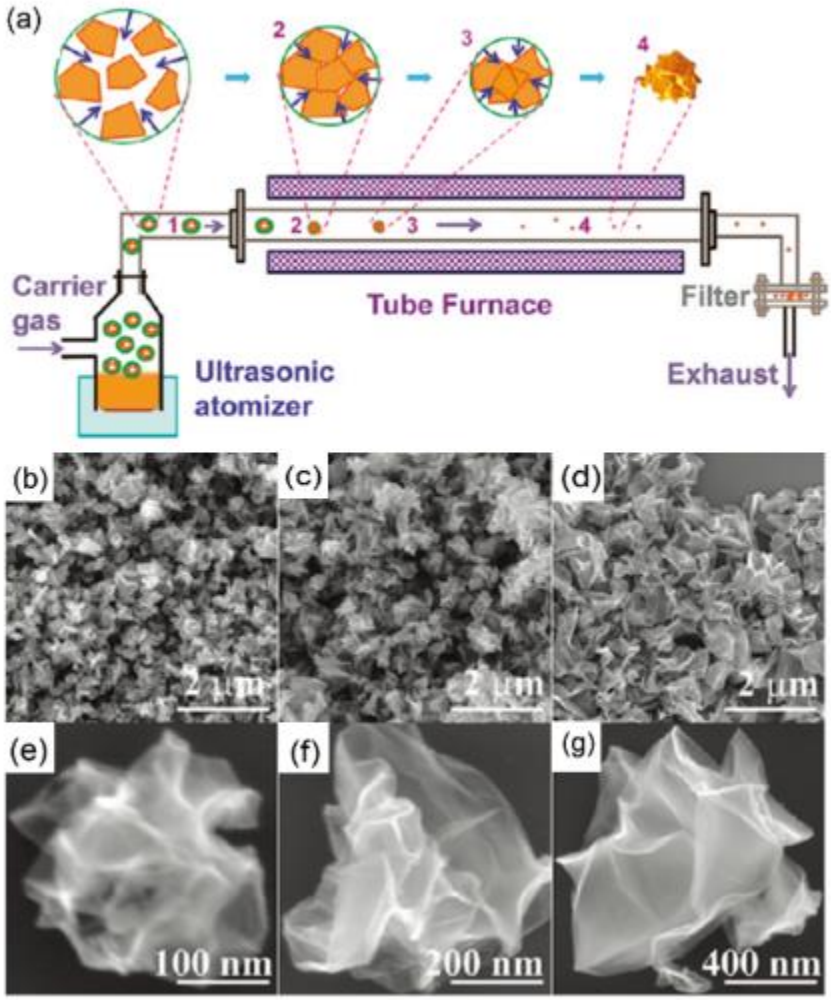

Fig. 1 (a) A schematic illustrations of the setup and the preparation of crumpled graphene balls. (b-d) SEM images of graphene crumpled balls prepared from different GO concentration, which were 0.2 mg/ml, 1 mg/ml, 5 mg/ml, respectively. (e-g) high magnification SEM images of b-d, respectively. Reproduced with permission.[6] Copyright 2011, American Chemical Society.

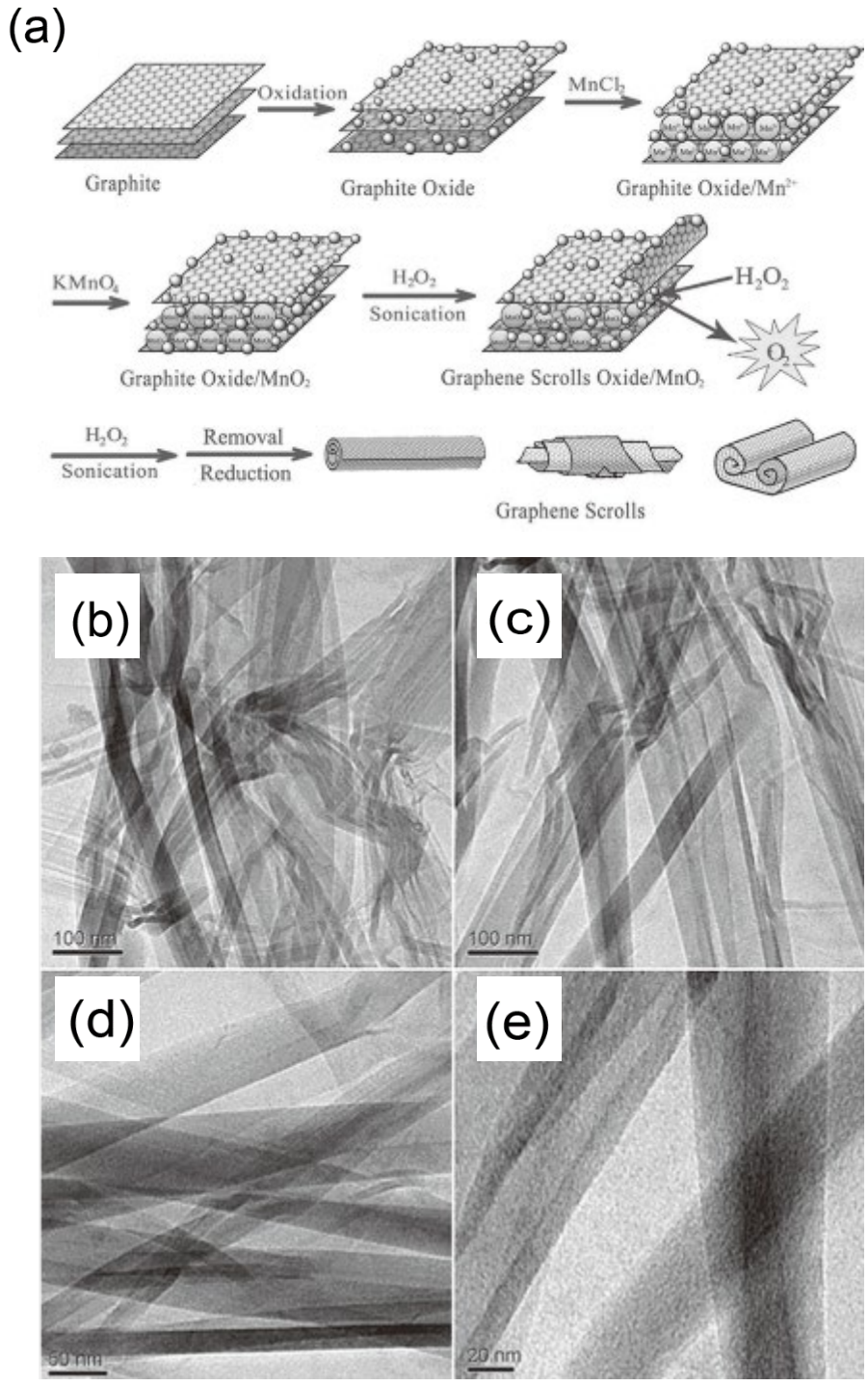

Fig. 2 (a) A schematic illustration of the preparation of graphene scrolls via microexplosion method. (b-e) TEM images of the obtained graphene scrolls with different magnification. Reproduced with permission.[77] Copyright 2011, Wiley-VCH.

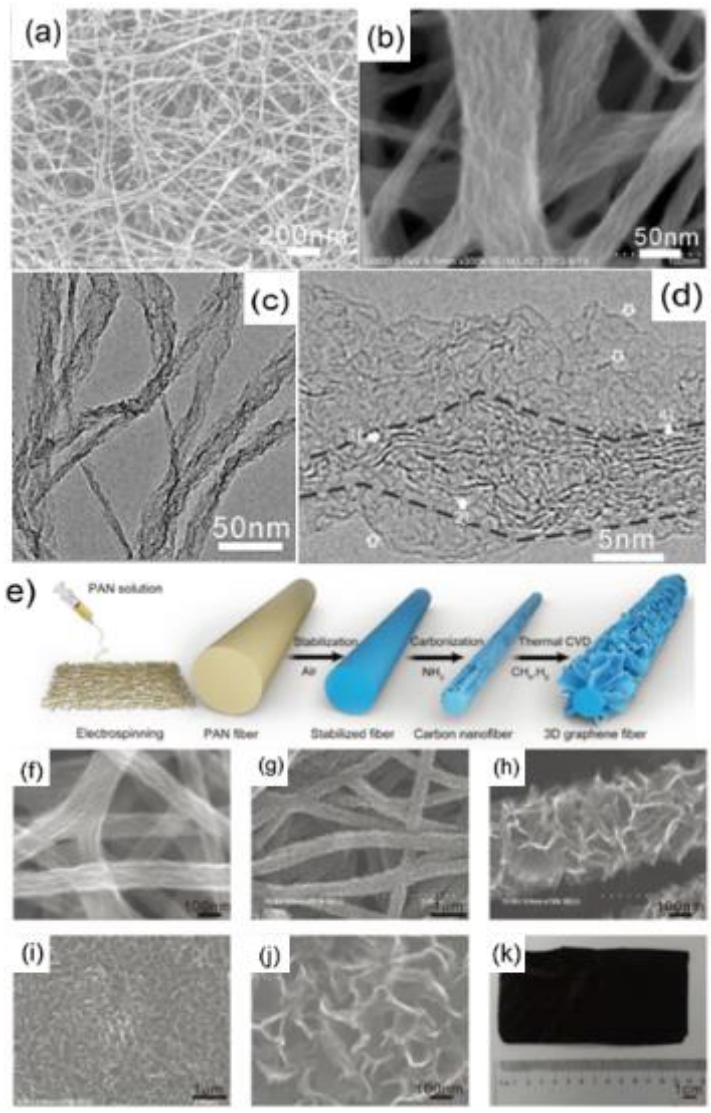

Fig. 3 (a) Low magnification SEM images of carbon nanofibers. (b) High magnification SEM images of carbon nanofibers with surface graphene sheets. (c-d) TEM images of carbon nanofibers with surface graphene sheets. Reproduced with permission.[90] Copyright 2013, Royal Society of Chemistry. (e) A scheme for the preparation of graphene fibers. (f) SEM image of carbon nanofibers with surface graphene sheets. (g-h) SEM images of graphene fibers grown for 4 h with methane concentration of 11.1 %. (i-j) SEM images of graphene fibers grown for 10 h with methane concentration of 11.1 %. (k) An optical image of graphene fiber membrane. Reproduced with permission.[91] Copyright 2018, Wiley-VCH.

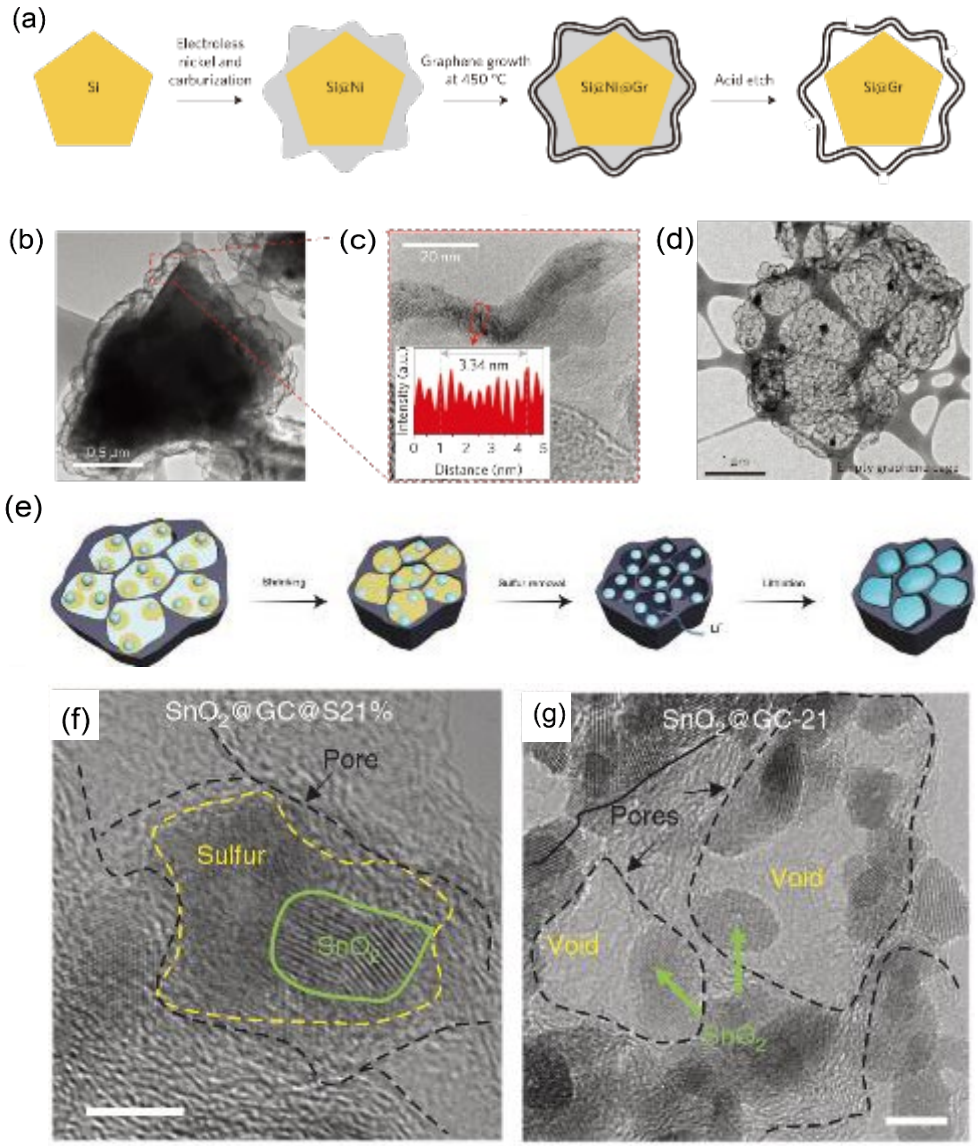

Fig. 4 (a) A scheme illustration for 3D graphene cage synthesis. (b) TEM image of graphene encapsulating Si microparticle. (c) HRTEM image showing layered structure of graphene cages. (d) Hollow graphene cage after the removal of Si microparticle. Reproduced with permission.[12] Copyright 2016, Springer Nature. (e) A scheme illustration for constructing graphene cage with optimal void space. (f) TEM images of SnO_2@graphene coated by sulfur with a weight ratio of 21%. (g) TEM images of SnO_2@graphene with rough preparation for comparison. Reproduced with permission.[106] Copyright 2018, Springer Nature.

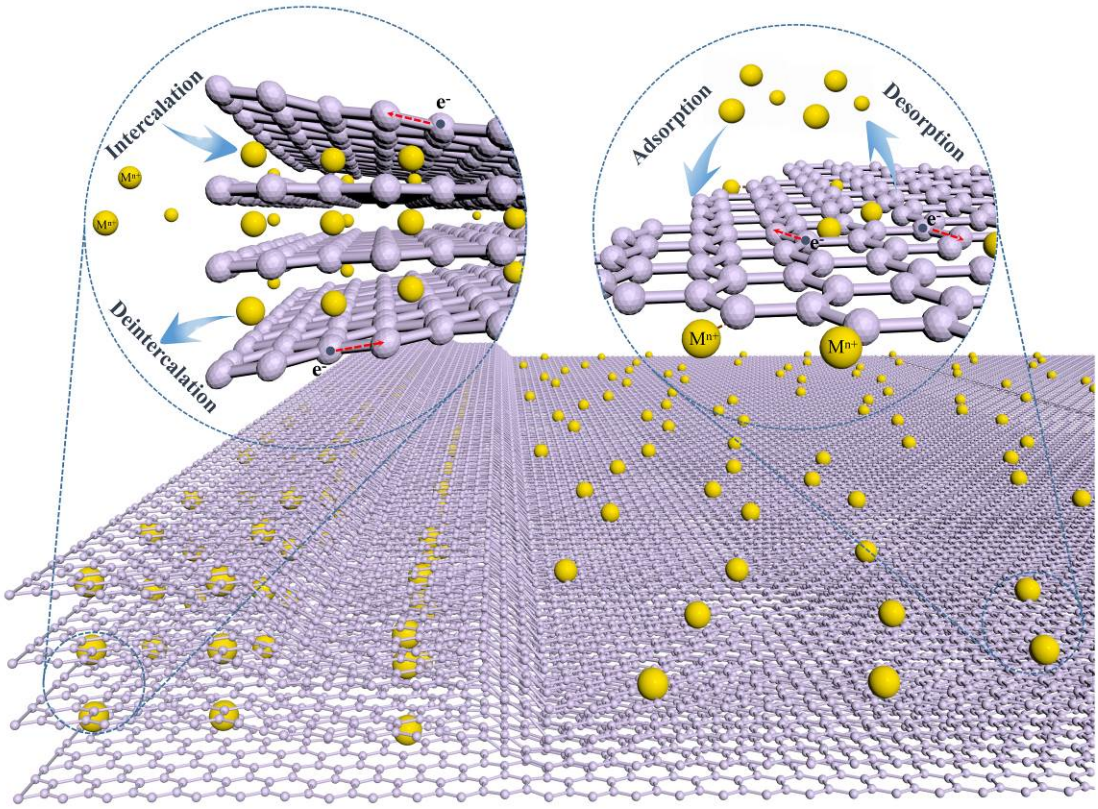

Fig. 5 Schematic illustrations of general mechanisms of metal-ion storage in graphene layers.

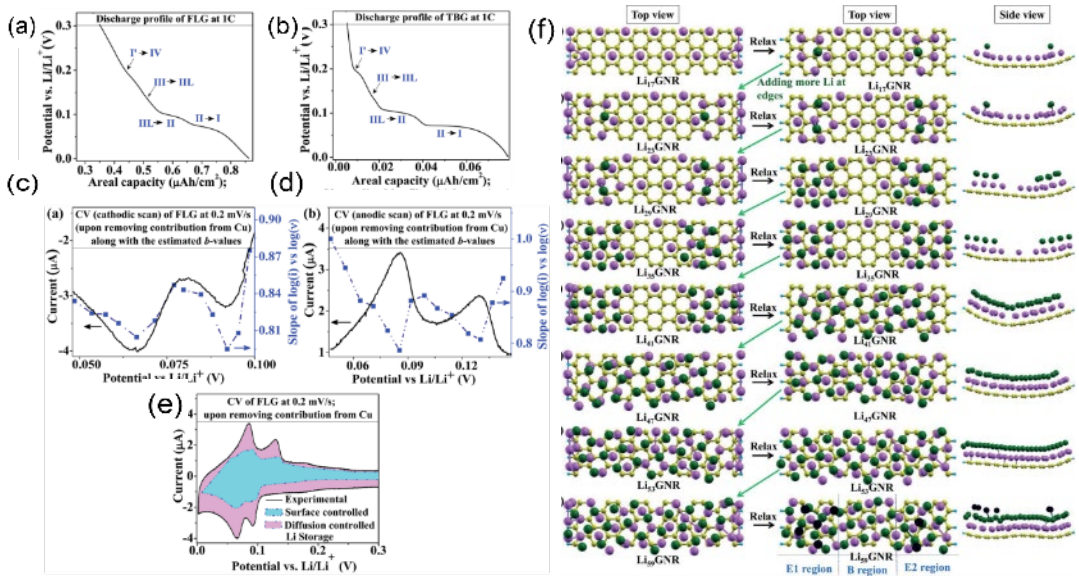

Fig. 6 (a) Discharge curves for few-layered graphene in the voltage window between 0.3 and 0.001 V (against Li/Li^+). (b) Discharge curves for graphite in the voltage window between 0.3 and 0.001 V (against Li/Li^+). (c-d) Cathodic and anodic CV scan

of few-layered graphene and the calculated slope value of log (i) *vs.* log (*v*). (e) The contributions of surface-controlled process and diffusion-controlled process. (f) A schematic illustration of the distributions of lithium ions on the graphene surface with increasing Li concentration. The yellow and cyan balls represent C and H atoms, respectively. The magenta, green, and black colored balls represent Li atoms that are in the 1st Li-layer, the 2nd Li-layer and the 3rd Li-layer above the graphene sheet, respectively. Reproduced with permission.[164] Copyright 2017, Royal Society of Chemistry.

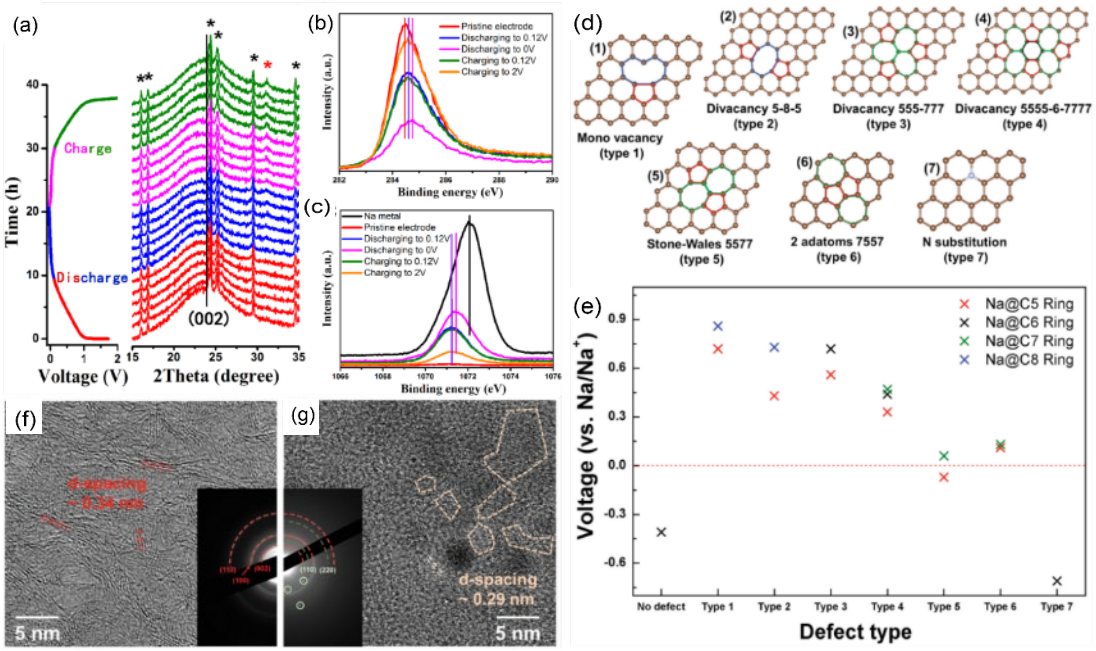

Fig. 7 (a) In-situ XRD patterns collected during first discharge/charge in the voltage window of 0 - 2 V with a current density of 0.05 C. (b) Ex-situ XPS of C 1s spectra. (c) Ex-situ XPS of Na 1s spectra. Reproduced with permission.[170] Copyright 2016, Elsevier. (d) Different types of defect sites in basal plane of graphene. (e) DFT calculation data for chemisorption energy of given effect site with sodium ions. (f) HRTEM image of sample before discharging. (g) HRTEM image of sample after discharging to 0.005 V. Reproduced with permission.[171] Copyright 2015, Wiley-VCH.

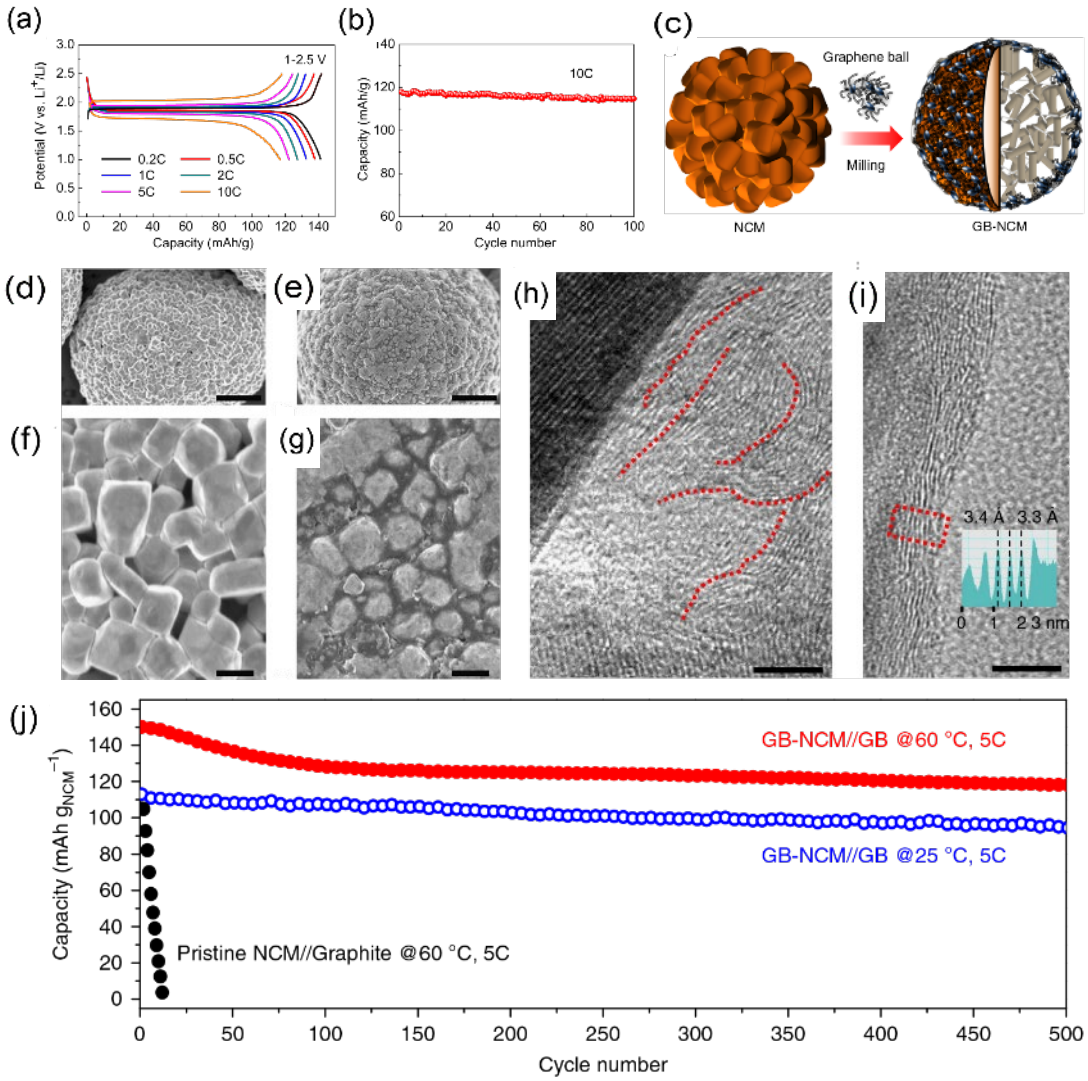

Fig. 8 (a) Rate performance of a flexible LTO/LFP/GF full battery. (b) Cyclic performance of LTO/LFP/GF full battery at 10 C. Reproduced with permission.[199] Copyright 2012, National Academy of Sciences. (c) Schematic illustration of the GB coating onto NCM. (d,f) SEM images of pristine NCM. (e,g) SEM images of NCM after graphene ball coating. (h-i) Graphene layers located between or coated along primary particles of $LiNi_{0.6}Co_{0.1}Mn_{0.3}O_2$. (j) Cycle life of GB-NCM/GB full-cell at 60 °C and 25 °C at 5 C. Reproduced with permission.[209] Copyright 2017, Springer Nature.

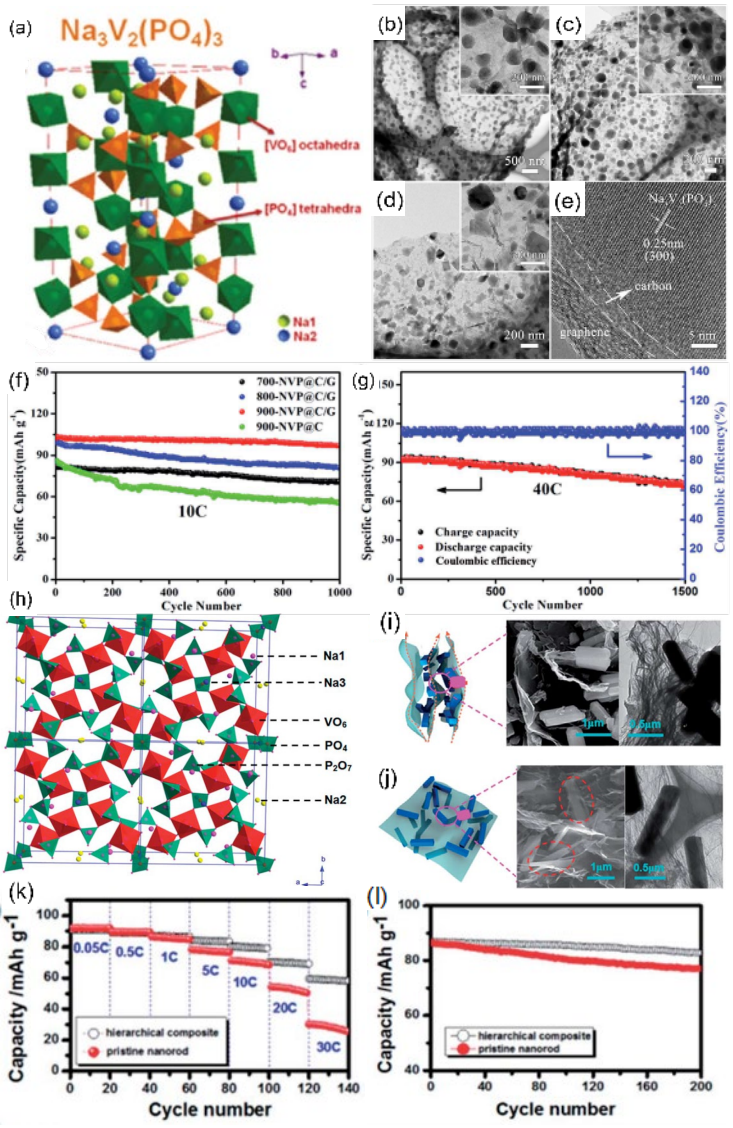

Fig. 9 (a) Crystal structure of $Na_3V_2(PO_4)_3$. Reproduced with permission.[233] Copyright 2015, Wiley-VCH. (b-e) SEM images and TEM images of 3D graphene/C/NVP composites. (f-g) Sodium storage properties of 3D graphene/C/NVP composites at 10 C and 40 C. (h) Crystal structure of $Na_7V_4(P_2O_7)_4(PO_4)$. Reproduced with permission.[232] Copyright 2017, Royal Society of Chemistry. (i-j) SEM images and TEM images of 3D graphene/C/$Na_7V_4(P_2O_7)_4(PO_4)$ composites. (k-l) Sodium storage properties of 3D graphene/C/$Na_7V_4(P_2O_7)_4(PO_4)$ composites. Reproduced with permission.[236] Copyright 2014, Royal Society of Chemistry.

Tables:

Table 1 Properties and applications of 3D graphene prepared by template-assisted CVD method.

No.	Template	Structure	Electrical and Mechanical property	Surface area	Applications	Ref.
1	Nickel foam	Graphene interconnected framework: pore size (hundreds of micrometers), porosity (~99.7%)	Conductivity: 10 S cm^{-1}, excellent mechanical robustness	850 m^2/g		10
2	Nickel nanoparticles	Graphene hollow spheres with abundant pores: diameter of graphene spheres (5 - 10 μm), pore size (up to 72 nm)		285.3 m^2/g	Biosensor	14
3	Nickel nanowires	Graphene hollow tubes: mean tube diameter (70 nm), length of tube (up to several micrometers)				8
4	Porous anodic aluminum oxide	Interconnected macroporous framework or graphene tubes: diameter of graphene nanotubes (110 nm)	Conductivity: 1290 S m^{-1}, low sheet electrical resistance: 0.11 Ω sq^{-1}		Heat transfer and thermal energy storage	74
5	Cage containing MOFs	Graphene tubes: diameter (tens of nanometers to sub-micrometers)		449 m^2/g	ORR catalyst	75
6	NaCl	Graphene hollow cubes: length of graphene cube unit (~10 μm)	Good flexibility and conductivity	1216 m^2/g	Supercapacitor	108
7	Silica spheres	Hollow graphene balls: diameter of graphene spheres (360 - 550 nm)			Lithium-sulfur batteries	126
8	Polystyrene balls	Mesoporous graphene nanoballs: mean pore diameter (4.27 nm)	Conductivity: 6.5 S cm^{-1}	508 m^2/g	Supercapacitor	127

9	Nanoporous copper	Duct-like nanoporous graphene film: pore size (500 - 800 nm)	Sheet electrical resistance: 23.3 Ω sq^{-1}, high flexibility	586.3 m^2/g	Supercapacitor	128
10	MgO flakes	Graphene honeycomb like framework containing nanocages: size of cages (5 - 10 nm), lateral size of framework (2 μm), thickness of framework (50 nm)	Conductivity: 54 S cm^{-1}	240 m^2/g	OER catalyst	129

Table 2 The configurations and performances of AIBs, PIBs and Mg-ion batteries.

No.	Type	Anode	Cathode	Power density & Energy density	Specific capacity	Ref.
1	AIB	Al foil	Porous graphene foam		Volumetric capacities up to 12.2 mA h cm^{-3}; gravimetric capacity up to 151 mA h g^{-1} after 100 cycles	57
2	AIB	Al foil	Graphene Microflo-wer	Energy density: 40 W h kg^{-1}, power density: 3000 W kg^{-1}	100 mA h g^{-1} at 5 A g^{-1} after 5000 cycles	162
3	AIB	Al foil	rGO/SnS_2	Energy density: 241 W h kg^{-1}	112 mAh g^{-1} at 10 A g^{-1}	54
4	AIB	Al foil	Graphene nanoribb-ons @ porous graphene		123 mA h g^{-1} at 50 A g^{-1} after 10000 cycles; high rate performance with a capacity of 111 mA h g^{-1} at 80 A g^{-1}	55
5	AIB	Al foil	3D graphene mesh		57 mA h g^{-1} at 40 C after 200 cycles	56
6	PIB	Nitrogen doped graphene foam	K foil		210 mA h g^{-1} after 100 cycles	172
7	PIB	Phospho-rus and oxygen dual-doped graphene	K metal		474 mA h g^{-1} at 50 mA g^{-1} after 50 cycles and 160 mA h g^{-1} at 2 A g^{-1} after 600 cycles	173

8	PIB	F-doped graphene foam	K foil		165.0 mA h g^{-1} at 0.5 A g^{-1} after 200 cycles and 301.9 mA h g^{-1} at 0.05 A g^{-1}	174
9	PIB	Sb_2S_3 particles/ graphene framework	$KVPO_4F$	Energy density: 166.3 W h kg^{-1}	548 mA h g^{-1} at 20 mA g^{-1} and 340 mA h g^{-1} at 10 A g^{-1}	238
10	PIB	MoS_2/ rGO	K foil		381 mA h g^{-1} after 100 cycles; 679 mA h g^{-1}at 20 mA g^{-1}, 178 mA h g^{-1} at 500 mA g^{-1}	240
11	MIB	Activated carbon	rGO/ V_2O_5 aerogel		100 mA h g^{-1} at 1 A g^{-1} after 200 cycles;	243
12	MIB	FeVO4 $0.9H_2O$/ graphene	Mg-OMS-1	Energy density: 58.5 W h kg^{-1} , power density: 50.8 W kg^{-1}	52.8 mA h g^{-1} at 0.1 A g^{-1} after 100 cycles (97% retention)	263
13	MIB	Mg foil	Co_3O_4/ graphene		16 mA h g^{-1} in the initial discharge	246